Michigan Tech Publications

1-1-2021

Degradation issues and stabilization strategies of protonic ceramic electrolysis cells for steam electrolysis

Hanrui Su
Michigan Technological University, hanruis@mtu.edu

Yun Hang Hu
Michigan Technological University, yunhangh@mtu.edu

Recommended Citation

REVIEW

Degradation issues and stabilization strategies of protonic ceramic electrolysis cells for steam electrolysis

Hanrui Su | Yun Hang Hu

Department of Materials Science and Engineering, Michigan Technological University, Houghton, Michigan, USA

Correspondence
Yun Hang Hu, Department of Materials Science and Engineering, Michigan Technological University, 1400 Townsend Drive, Houghton, MI 49931-1295, USA.
Email: yunhangh@mtu.edu

Abstract

Protonic ceramic electrolysis cells (PCECs) are attractive electrochemical devices for converting electrical energy to chemicals due to their high conversion efficiency, favorable thermodynamics, fast kinetics, and inexpensive materials. Compared with conventional oxygen ion-conducting solid oxide electrolysis cells, PCECs operate at a lower operating temperature and a favorable operation mode, thus expecting high durability. However, the degradation of PCECs is still significant, hampering their development. In this review, the typical degradations of PCECs are summarized, with emphasis on the chemical stability of the electrolytes and the air electrode materials. Moreover, the degradation mechanism and influencing factors are assessed deeply. Finally, the emerging strategies for inhibiting long-term degradations, including chemical composition modifications and microstructure tuning, are explored.

KEYWORDS
high-temperature electrolysis, hydrogen production, proton conductors, solid oxide cells, water splitting

1 | INTRODUCTION

Hydrogen (H_2) is a clean and flexible energy carrier.[1] Currently, H_2 is produced by steam reforming of fossil fuels (natural gas, coal, and oil) because of the high efficiency and low cost.[2,3] However, these fossil fuels are nonrenewable and the undesirable carbon monoxide (CO) and carbon dioxide (CO_2) cause several environmental issues.[4] Electrolyzing water (H_2O) to generate H_2 is technologically promising and economically viable for H_2 production.[5,6] Low-temperature (25-160°C) water electrolysis devices have been widely studied, such as the proton exchange membrane electrolysis cell (PEMEC) and the alkaline electrolysis cell (AEC). However, they require

high cell voltages (1.7-1.9 V) and precious metal electrocatalysts to achieve an acceptable hydrogen production rate.[5] In contrast, the solid oxide electrolysis cell (SOEC) can operate at elevated temperatures (>500°C), leading to high conversion efficiency, less electrical energy requirement, and inexpensive cell materials.[7] Moreover, SOECs can work with variable feedstock gases, conduct a reversible operation, or combine with heat networks.

As shown in Figure 1A,B, based on the types of electrolytes, SOECs can be classified as the oxygen ion-conducting SOEC and the proton-conducting SOEC. The proton-conducting SOEC, which is also termed protonic ceramic electrolysis cell (PCEC), has attracted more research interest recently due to the potential lower
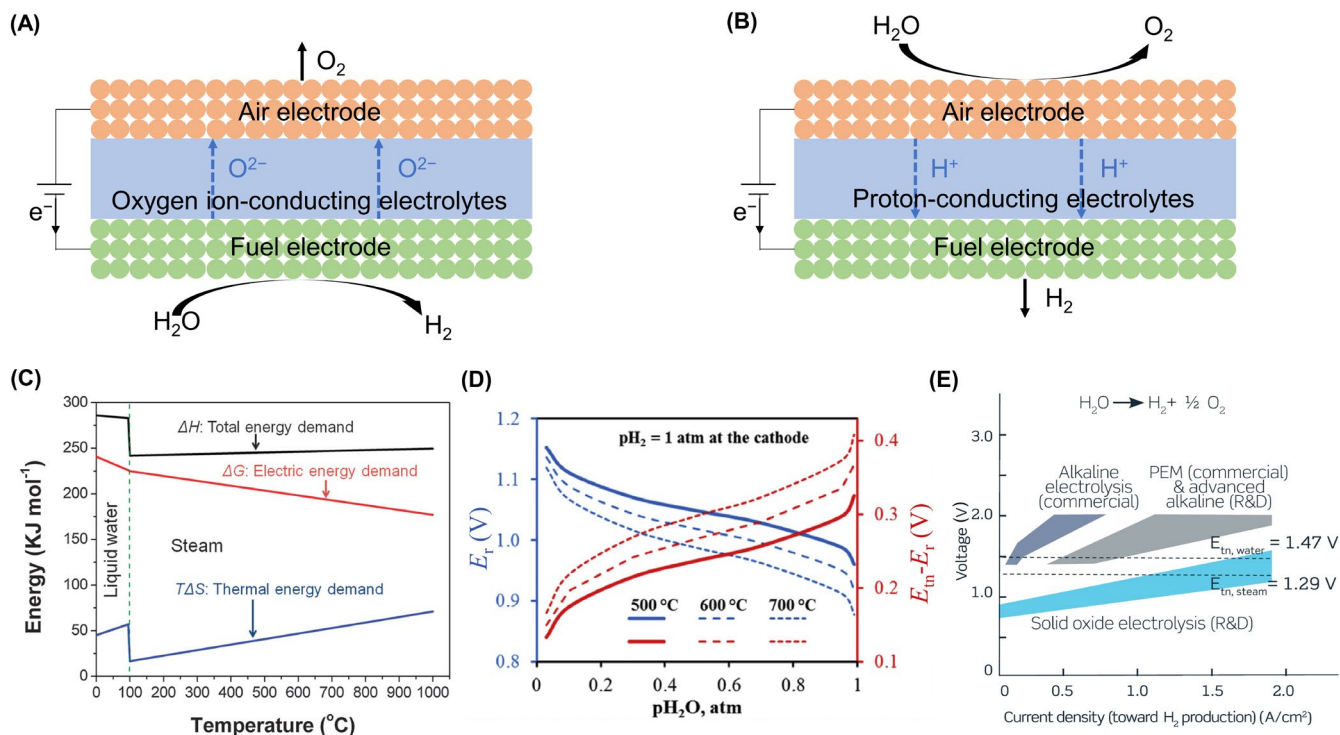
FIGURE 1 Schematics of (A) oxygen ion-conducting SOEC and (B) PCEC. (C) Electric, thermal, and total energy demand for H_2O electrolysis at a steam pressure of 1 atm as a function of temperature. Reprinted with permission from Ref.[8] Copyright 2014 Royal Society of Chemistry. (D) Reversible potential (E_r) and overvoltage (differences between E_{tn} and E_r) value for PCECs depending on pH_2O in an oxidizing atmosphere. Reprinted with permission from Ref.[18] Copyright 2019 Elsevier. (E) Typical performance ranges for diverse technologies for H_2O electrolysis. Reprinted with permission from Ref.[7] Copyright 2020 The American Association for the Advancement of Science

operating temperature (500-700°C) and ease in gas separation.[8,9] In a SOEC, the steam was fed to produce H_2 at the fuel electrode, which requires a gas separator to obtain pure and dry hydrogen. In a PCEC, steam electrolysis occurs at the air electrode (Equation 1), and then, the generated protons migrate to the fuel electrode for producing pure H_2 by applying an external voltage (Equation 2). This greatly simplifies the systems and lowers the operation cost. Moreover, the proton conductivity was higher than that of oxygen ions at lower temperatures.[8,9] The lower operating temperatures provide benefits, such as cheaper interconnect and sealing materials, rapid thermal cycling, and potential higher durability and reliability.

$$\text{Air electrode: } H_2O \rightarrow 2H^+ + 2e^- + \frac{1}{2}O_2 \quad (1)$$

$$\text{Fuel electrode: } 2H^+ + 2e^- \rightarrow H_2 \quad (2)$$
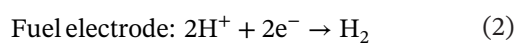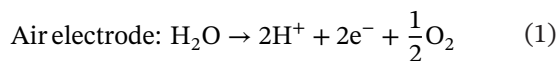
However, the SOEC technology suffers from fast material degradation and limited long-term stability. For SOECs based on oxygen ion-conducting yttria-stabilized zirconia (YSZ) electrolytes, these degradations are mainly

caused by the contamination of impurities (such as SiO_2, Cr, and S), delamination of air electrode due to the higher partial pressure of oxygen gradient, and the coarsening and migration of nickel-based fuel electrodes.[7,10,11] Fortunately, great progresses were made in the past 15 years, tremendously decreasing the degradation rate by a factor of ~100.[7] For example, under practical operations conditions, the degradation rate of <0.5%/1000 h at −1 A cm^{-2} for 2000 hours operation was achieved.[12] Similar low degradation rate (0.3%-0.4%/1000 h) was reported for a SOEC with 34,000 hours operation at −0.6 A cm^{-2} current density.[13] These highly durable SOECs are comparable to the commercialized AECs or PEMECs with a stack lifetime up to 90,000 hours and a degradation rate <1% per 1000 hours.[14]

As for newly developed SOECs, PCECs are expected to have a higher durability than conventional oxygen ion-conducting SOECs due to the relatively low operating temperatures, strong interface/adhesion between electrodes and electrolytes, and the better operation mode.[9] In principle, the PCECs avoid the issues of Ni oxidation/coarsening in the fuel electrode and the delamination in air electrode, which are the main factors causing the degradation of oxygen ion-conducting

SOECs.[15] However, various degradations of PCECs were observed in durability tests under different conditions. Compared with oxygen ion-conducting SOECs, PCECs possess the distinct degradation mechanisms and behaviors, which deserve a comprehensive summary. Although there are several excellent comprehensive reviews on PCECs[5,8,9,15-20] and topic reviews on the design of electrode materials for PCECs,[21-25] rare assessments focus on the degradation of PCECs for steam electrolysis. This has stimulated us to write this review on the degradation of PCECs, with emphasis on degradation mechanisms and mitigation strategies.

2 | FUNDAMENTALS OF PCECS FOR STEAM ELECTROLYSIS

2.1 | Thermodynamics of high-temperature steam electrolysis

The overall reaction of water splitting was given by Equation 3

$$H_2O \rightarrow H_2 + \frac{1}{2}O_2, \ \Delta H^o_{298} = 229.8 \, kJ \cdot mol^{-1} \quad (3)$$
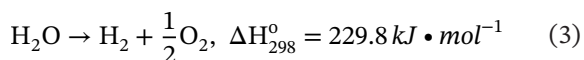
The thermodynamics of steam electrolysis was shown in Figure 1C. The total energy demand (ΔH) is the sum of the electric energy demand (ΔG) and the thermal energy demand ($T\Delta S$). The electric energy demand is compensated by the thermal energy demand with increasing temperature, indicating that relatively lower electricity is required for high-temperature steam electrolysis than low-temperature liquid water electrolysis technologies (eg, AEC or PEMEC).

The reversible potential (E_r) is the theoretical minimum potential required for water electrolysis, which can be expressed by the Nernst equation (Equation 4).

$$E_r = E^0 + \frac{RT}{2F} \ln \frac{P_{H_2} P_{O_2}^{1/2}}{P_{H_2O}} \quad (4)$$

In this equation, E^0 represents standard potential, F Faraday's constant, R the universal gas constant, and T the temperature, while P_{H_2O}, P_{H_2}, and P_{O_2} are the partial pressures of H_2O, H_2, and O_2 at the electrodes, respectively. E^0 is 1.23 V for 1 atm of the H_2O at 25°C. The E_r decreases with increasing temperature, and thus, the minimum applied voltage for the high-temperature electrolysis is lower than the low-temperature electrolysis.[5,18] Higher partial pressure of H_2O also results in lower E_r, which is beneficial for the realization of

higher overvoltage to achieve higher current densities (Figure 1D).[18]

The thermoneutral potential (E_{tn}) represents the standard operation mode of high-temperature steam electrolysis, which is defined as Equation 5.

$$E_{tn} = \frac{\Delta H}{2F} \quad (5)$$

At the thermoneutral potential, the heat required for the endothermic electrolysis process is compensated by the power produced by the cell at a given current density and temperature. There is no external heating (or cooling) required for the operation under this condition if no heat loss to the surroundings. As shown in Figure 1E, a SOEC can obtain a current density of ~1.5 A cm^{-2} at the E_{tn} for the steam electrolysis (1.29 V, 800°C), while a typical AEC or PEMEC only attains a current density of ~0.5 A cm^{-2} when operated at the E_{tn} for the liquid water electrolysis (1.47 V, 25°C). Therefore, the operation cost and capital cost of a SOEC are lower if the degradation challenges are successfully addressed.[7]

Under practical operation, the cell voltage (E) is the sum of the reversible potential (E_r) and the overpotentials due to the polarization loss (E_p), concentration loss (E_p), and ohmic loss (E_o) (Equation 6).[26] Thus, the practical electrolysis cells are operated at the potentials slightly higher than E_{tn}.

$$E = E_r + E_p + E_c + E_o \quad (6)$$

The current efficiency or Faradaic efficiency (η_F) is defined as the ratio of measured to theoretical hydrogen production rate (Equation 7). The Faradaic efficiency for H_2O electrolysis in SOECs is close to 100%.[5] However, the PCECs historically suffered from the low Faradaic efficiency due to the p-type electronic leakage of the electrolyte.[15]

$$\eta_F = \frac{n_{H_2}}{I/2F} \quad (7)$$

where n_{H_2} and I are the hydrogen production rate and the applied current, respectively.

The energy conversion efficiency (η_{LHV}) is defined based on the lower heating value (LHV) of H_2 (Equation 8).[27]

$$\eta_{LHV} = \frac{n_{H_2} \Delta H_{LHV}}{EI} \quad (8)$$

where ΔH_{LHV} is the LHV reaction enthalpy for steam electrolysis (241.8 kJ mol^{-1}) and E the applied voltage or cell voltage. For an advanced PCEC, the overall

η_{LHV} >97% can be achieved at a current density of -1 A cm^{-2}.[27]

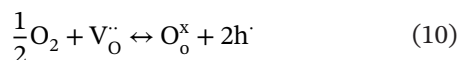## 2.2 | Mechanisms of proton transport

For a perovskite oxide proton conductor, the proton $(OH_O^{\cdot})$ is generated via a hydration process under humid and reducing conditions, which is influenced by both pH_2O, the oxygen vacancy $(V_O^{\cdot\cdot})$ concentration, and the lattice oxygen (O_o^x) concentration in Kröger-Vink notation (Equation 9). Since the reaction is exothermic, the proton concentration decreases with increasing temperature.[15,24,28]

$$H_2O + V_O^{\cdot\cdot} + O_o^x \leftrightarrow 2OH_O^{\cdot} \qquad (9)$$

Two mechanisms were proposed to describe the proton transport process in the perovskite-type proton conductors[28,29]: (1) the Grotthuss mechanism that the protons migrate via reorientation of the proton and the formation and cleavage of bonds with the adjacent lattice oxygen (Figure 2A), and (2) the vehicle mechanism which the protons are firstly bounded with oxygen ions to form hydroxide ions and then diffuse through oxygen vacancies (Figure 2B).

Under humid and oxidizing conditions, increasing pO_2 led to a decline in oxygen vacancy concentration by parasitic oxidation reaction (Equation 10). A proton conductor can take up protons via a hydrogenation process (Equation 11).

$$\frac{1}{2}O_2 + V_O^{\cdot\cdot} \leftrightarrow O_o^x + 2h^{\cdot} \qquad (10)$$

$$H_2O + 2O_o^x + 2h^{\cdot} \leftrightarrow 2OH_O^{\cdot} + \frac{1}{2}O_2 \qquad (11)$$

For the layered materials, H_2O is more favorable for insertion at the interstitial sites (Equation 12),[25] where the OH occupies the interstitial site and H attaches to the lattice oxygen.

$$H_2O + O_o^x \leftrightarrow OH_O^{\cdot} + OH_i' \qquad (12)$$
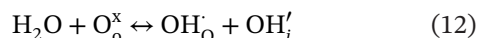
The increase in pH_2O could decrease both oxygen ionic and p-type electronic conductivities according to Equations 9 and 11. For example, the measured protonic, oxygen ionic, and electron-hole transport numbers of a typical $BaZr_{0.7}Ce_{0.2}Y_{0.1}O_{3-\delta}$ (BZCY72) proton conductor are dependent on pO_2 and pH_2O at intermediate temperature (600 and 700°C) (Figure 2C-H).[17] The protonic conductivity dominated under higher humid and lower

oxygen partial pressure conditions at the lower temperature, the oxygen ion conductivity under the dry and reducing conditions, and the hole conductivity under the conditions of a dry and oxidizing atmosphere at a higher temperature. The transport properties of proton conductors, which are affected not only by operating temperature and atmosphere but also by the material composition and polarization current density, play a vital role in achieving large current density, high efficiency, and excellent durability in PCECs.

2.3 | Mechanisms of oxygen evolution reaction (OER) at the air electrode

Low OER activity has been considered as a limiting factor in PCEC performance, especially at low temperatures.[8,9,15] He et al[30] proposed a mechanism for a $Sm_{0.5}Sr_{0.5}CoO_{3-\delta}$ (SSC)-$BaZr_{0.3}Ce_{0.5}Y_{0.2}O_{3-\delta}$ (BZCY35) composite air electrode (Table 1), including the surface dissociative adsorption of water, the formation and desorption of O_2 along with the charge transfer, and the proton migration to triple-phase boundary (TPB). The TPB is the area where gas, electrode, and electrolyte meet simultaneously. They revealed that the water ionization and proton transfer from the electrode surface to the electrolyte constituted the rate-limiting steps in the electrolysis by electrochemical impedance spectroscopy (EIS) measurements. In contrast, Tian et al[31] suggested a bulk-surface hybrid mechanism for a $Pr_{1.75}Ba_{0.25}NiO_{4+\delta}$ air electrode with triple-conducting properties (simultaneously conduction of H^+, O^{2-}, e^-) (Table 1). Namely, the water dissociation and proton incorporation are faster, whereas the rate-limiting step is the reduction of surface O^-. This was attributed to the slower catalytic capability for the reduction of surface O^-. Different from oxygen ion-conducting SOEC, the water participates in both the OER, hydration, and proton transport in the PCECs.[15] Therefore, the air electrode with higher proton conductivity enables the OER to occur at the surface of the air electrode instead of limited TPB, leading to the large enhancement in the overall OER performance.

3 | MATERIALS OF PCECS FOR STEAM ELECTROLYSIS

For comparison purpose, the performances and durability of state-of-the-art PCECs were summarized in Figure 3 and Table 2. In general, the current density at E_{tn} (~1.3 V) increases with increasing temperature. Many PCECs can achieve high electrolysis current densities (1 A cm^{-2}) at a lower temperature (~600°C), which are comparable to the current densities at 800°C of oxygen conducting SOECs.[5]
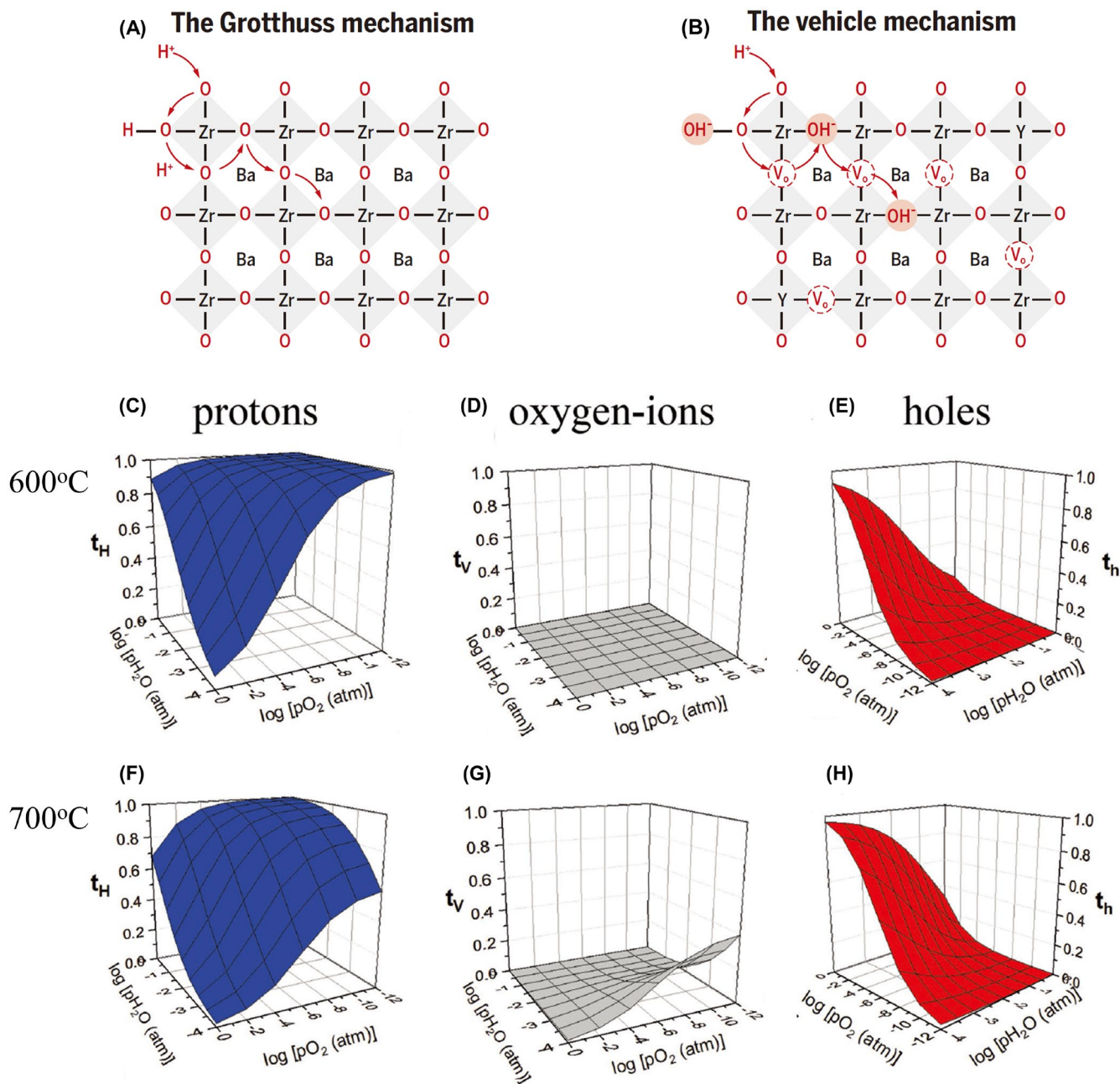
FIGURE 2 Schematics of two proton conduction mechanisms in a $BaZrO_3$-based perovskite oxide. (A) The Grotthuss mechanism; (B) The vehicle mechanism. Reprinted with permission from Ref.[29] Copyright 2020 The American Association for the Advancement of Science. (C, F) Protonic, (D, G) oxygen ionic, and (E, H) electron-hole transport numbers as functions of pO_2 and pH_2O at different temperatures for BZCY72 proton conductor. Reprinted with permission from Ref.[17] Copyright 2018 John Wiley and Sons

The best performance was achieved using a pulsed laser deposition (PLD) $PrBa_{0.5}Sr_{0.5}Co_{1.5}Fe_{0.5}O_{5+\delta}$ (PBSCF) as the air electrode and $BaZr_{0.4}Ce_{0.4}Y_{0.1}Yb_{0.1}O_{3-\delta}$ (BZCYYb4411) as the electrolyte, yielding a remarkable current density of 1.92 A cm^{-2} at 600°C and 1.3 V.[32]

However, only a few studies have evaluated the long-term durability of PCECs with a duration time above 1000 hours (Figure 3B). The longest record to date for a lab-scale PCEC was reported by Zhou et al,[33] namely, the

single cell with the $PrBa_{0.8}Ca_{0.2}Co_2O_{5+\delta}$ (PBCC) air electrode and the $BaZr_{0.1}Ce_{0.7}Y_{0.1}Yb_{0.1}O_{3-\delta}$ (BZCYYb1711) electrolyte exhibited a low degradation rate (3.3%/1000 h) under 1833 hours continuous operation at 1 A cm^{-2} and 650°C. In this section, the chemical stability and compatibility, morphological stability of electrolyte materials, electrode materials, and their interface in PCECs were systematically discussed. The modification strategies reported in the literature were also highlighted.

TABLE 1 The main elementary steps for reactions at the air electrodes of PCECs

Type of reaction	$Sm_{0.5}Sr_{0.5}CoO_{3-\delta}$-$BaZr_{0.3}Ce_{0.5}Y_{0.2}O_{3-\delta}$[30]	$Pr_{1.75}Ba_{0.25}NiO_{4+\delta}$[31]
H_2O adsorption	$H_2O_{(g)} \leftrightarrow H_2O_{ad}$	$H_2O_{(g)} \leftrightarrow H_2O_{ad}$
H_2O dissociation	$H_2O_{ad} \leftrightarrow H^{\cdot}_{ad} + OH'_{ad}$	$H_2O_{ad} \leftrightarrow H^{\cdot}_{ad} + OH'_{ad}$
Hydroxyl dissociation	$OH'_{ad} \leftrightarrow H^{\cdot}_{ad} + O''_{ad}$	$OH'_{ad} \leftrightarrow H^{\cdot}_{ad} + O''_{ad(high)}$
Proton incorporation		$H^{\cdot}_{ad} + O^x_o \leftrightarrow OH^{\cdot}_{o(el)}$
Proton diffusion	$H^{\cdot}_{ad} \leftrightarrow H^{\cdot}_{(tpb)}$	$OH^{\cdot}_{o(el)} \leftrightarrow OH^{\cdot}_{o(int)}$
Proton transfer	$H^{\cdot}_{(tpb)} \leftrightarrow H^{\cdot}_{(el)}$	$OH^{\cdot}_{o(int)} + O^x_{o(e)} \leftrightarrow O^x_{o(el)} + OH^{\cdot}_{o(e)}$
First charge transfer	$O''_{ad} + h^{\cdot} \leftrightarrow O'_{ad}$	$O''_{ad(high)} + h^{\cdot} \leftrightarrow O'_{ad(high)}$
Oxygen surface diffusion		$O'_{ad(high)} \leftrightarrow O'_{ad(low)}$
Second charge transfer	$O'_{ad} + h^{\cdot} \leftrightarrow O_{ad}$	$O'_{ad(low)} + h^{\cdot} \leftrightarrow O_{ad}$
Oxygen association desorption	$2O_{ad} \leftrightarrow O_{2(g)}$	$2O_{ad} \leftrightarrow O_{2(g)}$

Abbreviations: ad, adsorbed; e, electrolytes; el, electrode; g, gas; high or low, the species at high or low concentration location; int, interface; tpb, triple-phase boundary.
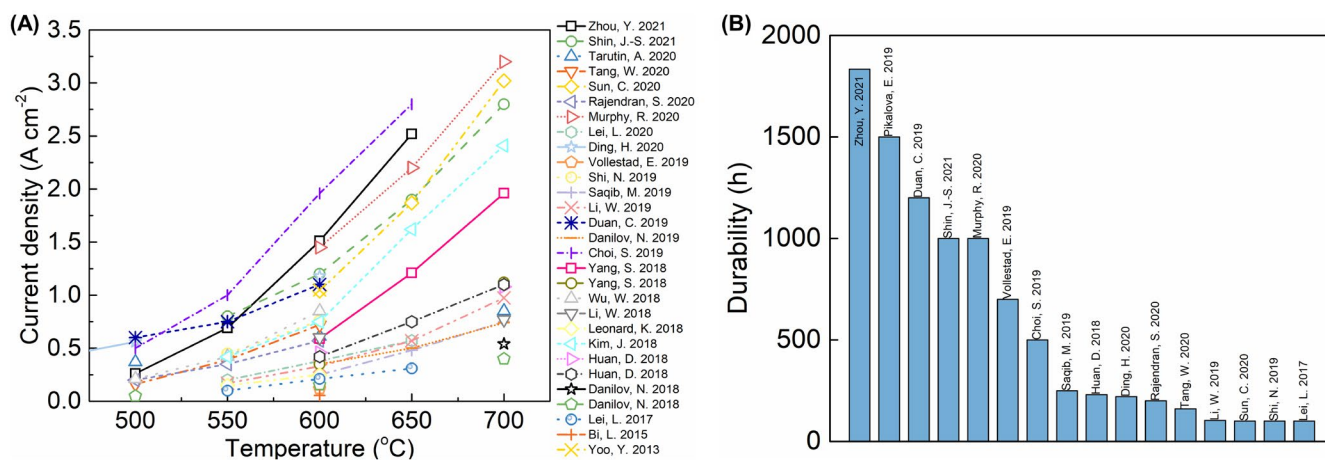

FIGURE 3 Performance and durability comparison of state-of-the-art PCECs. (A) Current density comparison at 1.3 V as a function of temperature. (B) Duration of stability test

3.1 | Proton-conducting electrolytes

The state-of-the-art ceramic proton conductors are ABO_3-type perovskites based on the barium cerate ($BaCeO_3$) and barium zirconate ($BaZrO_3$),[15,34] which exhibited high concentrations of proton charge carriers and proton conductivity due to their high hydration capability.[17] In general, $BaZrO_3$ possesses higher thermodynamic stability, while $BaCeO_3$ shows higher proton conduction, less parasitic electronic conduction, and higher sinterability. Therefore, most proton conductors are their combinations as solid solutions. Furthermore, to increase the degree of hydration and proton conduction, the B-site can be partially substituted by acceptor dopants (such as Y, Yb) to create oxygen vacancies. Consequently, $BaZr_{1-x}Y_xO_{3-\delta}$ (BZY), $BaZr_{1-x-y}Ce_yY_xO_{3-\delta}$ (BZCY), and $BaZr_{1-x-y-z}Ce_yY_xYb_zO_{3-\delta}$ (BZCYYb) have become the most investigated electrolytes for PCECs.

3.1.1 | Degradation of proton-conducting electrolytes

Although the proton conductors containing Ba on the A-site typically exhibit high conductivity, they are unstable in the presence of CO_2 and steam due to the undesirable reactions between the A-site cation and process gases (Equations 13 and 14).

$$H_2O + Ba(Ce, Zr)O_3 \leftrightarrow Ba(OH)_2 + (Ce, Zr)O_2 \quad (13)$$

$$CO_2 + Ba(Ce, Zr)O_3 \leftrightarrow BaCO_3 + (Ce, Zr)O_2 \quad (14)$$
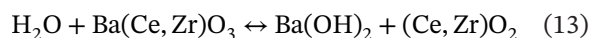
At a high steam concentration, the proton $OH^{\cdot}_O$ bond is transformed to the ionic bond with the formation of hydroxyl groups (OH^-), leading to the decomposition of the proton conductors. The equilibrium products of the above reactions are shown in Figure 4,[35] revealing that both

TABLE 2 Representative air electrodes of PCECs for steam electrolysis

Air electrodes	Cell configuration	Temp. (°C)	Testing conditions	Current density (A cm^{-2}) at 1.3 V	Stability	Reference
Perovskite oxide						
$Sm_{0.5}Sr_{0.5}CoO_{3-\delta}$	SSC-BZCY35| BZCY35 (20 μm) | Ni-BZCY35	600	Air (50% H_2O) vs. H_2	~0.20	Not reported	30
$Sm_{0.5}Sr_{0.5}CoO_{3-\delta}$	SSC| BZCY44 (1.5 mm) | Pt	600	Air (20% H_2O) vs. Ar (5% H_2)	~0.01	Not reported	72
$(La_{0.8}Sr_{0.2})_{0.98}MnO_{3-\delta}$	LSM-BCZI3 | BCZI3 (15 μm) | Ni-BCZI3	600	Air (20% H_2O) vs. H_2 (3% H_2O)	~0.12	No degradation for 60 h, 1.1 V at 700 °C	36
$(La_{0.75}Sr_{0.25})_{0.95}Mn_{0.5}Cr_{0.5}O_{3-\delta}$	LSCM-BCZYZ | BCZYZ (75 μm) | Ni-BCZYZ	700	N_2 (3% H_2O) vs. Ar (5% H_2)	~1.0	No degradation for 20 min, 2.0 V at 700 °C	69
$La_{0.6}Sr_{0.4}Co_{0.2}Fe_{0.8}O_{3-\delta}$	LSCF-BZY20| BZY20 (15 μm) | Ni-BZY20	600	Air (3% H_2O) vs. Ar (4% H_2)	0.055	No degradation for 80 h, 1.3 V at 600 °C	37
$La_{0.8}Sr_{0.2}Co_{0.7}Ni_{0.3}O_{3-\delta}$	LSCN| BZCY44 (24 μm) | Ni-BZCY44	600	Air (3% H_2O) vs. H_2 (3% H_2O)	1.09	No degradation for 60 h, 1.3 V at 600 °C	73
$Ba_{0.5}Sr_{0.5}Co_{0.8}Fe_{0.2}O_{3-\delta}$	BSCF-BZCY26| BZCY26 (15 μm) | Ni-BZCY26	600	Air (3% H_2O) vs. N_2 (50% H_2, 3% H_2O)	1.05	Not reported	74
$BaCo_{0.4}Fe_{0.4}Zr_{0.1}Y_{0.1}O_{3-\delta}$	BCFZY| BZCYYb1711 (12 μm) | Ni-BZCYYb1711	600	Air (10% H_2O) vs. Ar	~1.1	<30 mV/1000 h for 1200 h, 1.4 A cm^{-2} at 550 °C	27
$BaCo_{0.4}Fe_{0.4}Zr_{0.1}Y_{0.1}O_{3-\delta}$	SDC infiltrated BCFZY-BZCYYb1711| BZCYYb1711 (17 μm) | Ni-BZCYYb1711	600	Air (20% H_2O) vs. H_2	~0.25	0.2% for 250 h, 0.45 A cm^{-2} at 650 °C	75
$BaCo_{0.4}Fe_{0.4}Zr_{0.1}Y_{0.1}O_{3-\delta}$	BCFZY-BZCY36| BCZYSm (25 μm) | Ni-BCZYSm	600	Air (12% H_2O) vs. H_2 (3% H_2O)	0.37	Not reported	76
$Ba_{0}Zr_{0.6}Co_{0.4}O_{3-\delta}$	BZC-BZCY35| BZCY35 (20 μm) | Ni-BZCY35	700	Air (30% H_2O) vs. H_2	~0.55	Stable for 5 h, 1.3 V at 700 °C	77
$Ba_{0.5}La_{0.5}CoO_{3-\delta}$	BLC| BZCY(54)$_{8/9}$2 (12 μm)| Ni–SZCY	600	1% O_2/ 80% H_2O vs. Ar (1% H_2)	~0.25	Not reported	78
$PrNi_{0.5}Co_{0.5}O_{3-\delta}$	PNC| BCZYYbGd (25 μm) | Ni-BZCYYb1711	600	Air (20% H_2O) vs. H_2	0.57	1.7% for 200 h, 1.3 V at 600 °C	44
$PrNi_{0.5}Co_{0.5}O_{3-\delta}$	Hollow PNC fibers| BZCYYb4411 (15 μm) | Ni-BZCYYb4411	600	Air (10% H_2O) vs. Ar (10% H_2)	1.18	No degradation for 220 h, 1.4 V at 500 °C	42
$Sr_{0.9}Ce_{0.1}Fe_{0.8}Ni_{0.2}O_{3-\delta}$	SCFN| BZCYYb1711 (26 μm) | Ni-BZCYYb1711	600	Air (3% H_2O) vs. H_2	0.364	Stable for 120 h in fuel cell/electrolysis cycles at 550°C	79
Double perovskite oxide						
$BaGd_{0.8}La_{0.2}Co_2O_{6-\delta}$	BGLC| SZCY (20 μm) | Ni-SZCY	600	1% O_2/ 80% H_2O vs. Ar (1% H_2)	~0.15	Not reported	80
$Ba_{0.5}Gd_{0.8}La_{0.7}Co_2O_{6-\delta}$	BGLC5-BZCY72| BZCY72 (30 μm) | Ni-BZCY72	600	Ar (50% H_2O, 16.7% O_2) vs. Ar (16.7% H_2), 3 bar	~0.12	No degradation for 700 h, 62.5 mA cm^{-2} at 600 °C	50

TABLE 2 (Continued)

Air electrodes	Cell configuration	Temp. (°C)	Testing conditions	Current density (A cm^{-2}) at 1.3 V	Stability	Reference
$(PrBa_{0.8}Ca_{0.2})_{0.95}Co_2O_{6-\delta}$	PBCC95| BZCYYb4411 (20 μm) | Ni-BZCYYb4411	600	O_2 (20% H_2O) vs. H_2	0.72	No degradation for 160 h, 1.3 V at 500 °C	41
$PrBa_{0.8}Ca_{0.2}Co_2O_{5+\delta}$-$BaCoO_{3-\delta}$	PBCC-BCO| BZCYYb1711 (10 μm) | Ni-BZCYYb1711	600	Air (3% H_2O) vs. H_2 (3% H_2O)	1.51	3.3%/1000 h for 1833 h, 1 A cm^{-2} at 650 °C	33
$PrBa_{0.5}Sr_{0.5}Co_{1.5}Fe_{0.5}O_{5+\delta}$	3D PBSCF| BZCYYb1711 (20 μm) | Ni-BZCYYb1711	600	O_2 (12% H_2O) vs. Ar (5% H_2)	0.85	No degradation for 78 h, 1.6 V at 500 °C	59
$PrBa_{0.5}Sr_{0.5}Co_{1.5}Fe_{0.5}O_{5+\delta}$	PBSCF| PBSCF PLD| BZCYYb4411 (15 μm) | Ni-BZCYYb4411	600	Air (3% H_2O) vs. H_2 (3% H_2O)	**1.92**	Stable for 300 h, 1.3 V at 550 °C	32
$PrBa_{0.5}Sr_{0.5}Co_{1.5}Fe_{0.5}O_{5+\delta}$	PBSCF| BHCYYb3511 (10 μm) | Ni-BHCYYb3511	600	Air (3% H_2O) vs. H_2 (3% H_2O)	1.45	No degradation for 1000 h, 1 A cm^{-2} at 600 °C	43
$NdBa_{0.5}Sr_{0.5}Co_{1.5}Fe_{0.5}O_{5+\delta}$	NBSCF-BZCYYb1711| BZCYYb1711 (20 μm) | Ni-BZCYYb1711	600	Air (10% H_2O) vs. H_2 (10% H_2O)	0.75	No degradation for 60 h, 0.45 A cm^{-2} at 550 °C	81
$Sr_2Fe_{1.5}Mo_{0.5}O_{6-\delta}$	SFM-BZY20| BZY20 (16 μm) | Ni-BZY20	600	Air (3% H_2O) vs. N_2 (10% H_2)	0.21	Stable for 100 h, 1.3 V at 600 °C	82
$Sr_2Fe_{1.5}Mo_{0.5}O_{6-\delta}$	SFM-BZY20| BZY20 (18 μm) | Ni-BZCY17	600	Air (3% H_2O) vs. N_2 (20% H_2)	0.38	Stable for 10 h, 1.3 V at 600 °C	83
Ruddlesden–Popper perovskite or other types of oxides						
$Nd_{1.95}Ba_{0.05}NiO_{4+\delta}$	NBN-BZCD35| BZCD35 (15 μm) | Ni-BZCD35	600	Air (30% H_2O) vs. H_2 (3% H_2O)	0.155	Not reported	71
$Nd_{1.95}Ba_{0.05}NiO_{4+\delta}$	NBN-BZCD53| BZCD53 (50 μm) | Ni-BZCD53	700	Air (30% H_2O) vs. H_2 (3% H_2O)	0.54	Not reported	84
$Nd_{1.9}Ba_{0.1}NiO_{4+\delta}F_{0.05}$	NBNF| BZCYYb35 (25 μm) | Ni-BZCYYb35	600	Air (50% H_2O) vs. H_2 (3% H_2O)	0.36	Not reported	56
$La_2NiO_{4+\delta}$	LNO-BZCD35| BZCD35 (30 μm) | Ni-BZCD35	600	Air (30% H_2O) vs. H_2 (3% H_2O)	0.163	No degradation for 50 h, OCV at 600 °C	85
$La_{1.2}Sr_{0.8}NiO_{4-\delta}$	LSN| BCZY17 (16 μm) | Ni- BCZY17 FL| Ni- BCZY17	600	Air (90% H_2O) vs. H_2 (3% H_2O)	0.42	Not reported	86
$La_{1.2}Sr_{0.8}NiO_{4-\delta}$	LSN-BCZYYC2| BCZYYC2 (13 μm) | Ni- BCZYYC2 FL| Ni- BCZYYC2	600	Air (20% H_2O) vs. H_2 (3% H_2O)	0.59	No degradation for 60 h, 1.3 V at 700 °C	45
$La_{1.2}Sr_{0.8}NiO_{4-\delta}$	LSN infiltrated BCZYYC2| BCZYYC2 (13 μm) | Ni- BCZYYC2 FL| Ni- BCZYYC2	600	Air (20% H_2O) vs. H_2 (3% H_2O)	1.04	No degradation for 100 h, 1.3 V at 700 °C	49

(Continues)

TABLE 2 (Continued)

Air electrodes	Cell configuration	Temp. (°C)	Testing conditions	Current density (A cm⁻²) at 1.3 V	Stability	Reference
$(LaSr)_{0.9}Fe_{0.9}Cu_{0.1}O_{4+\delta}$	LSFCu-BZCY17| BZCY17 (211 μm) | LSFCu-BZCY17	700	N_2 (53.2% H_2O) vs. ambient air	~0.65	Stable for 10 h, OCV at 800 °C	87
$Pr_2NiO_{4+\delta}$	PNO-BZCY26| BZCY26 (20 μm) | Ni-BZCY26	600	Air (40% H_2O) vs. H_2	0.6	Not reported	57
$Pr_2NiO_{4+\delta}$	PNO| La$_2$Ce$_2$O$_7$| BZCYYb1711 (20 μm) | Ni-BZCYYb1711	600	Air (60% H_2O) vs. H_2	0.33	No degradation for 104 h, 0.4 A cm⁻² at 700 °C	48
$Pr_{1.2}Sr_{0.8}NiO_{4-\delta}$	PSN| BCZY17 (15 μm) | Ni- BCZY17 FL| Ni- BCZY17	600	Air (20% H_2O) vs. H_2 (3% H_2O)	0.35	No degradation for 40 h, 1.1 V at 700 °C	88
$Pr_{1.9}Ba_{0.1}NiO_{4+\delta}$	PB10N-BZCD35| BZCD35 (25 μm) | PB10N-BZCD35| Ni-BZCD35	600	Air (3% H_2O) vs. H_2 (3% H_2O)	0.295	Not reported	89
$Pr_{1.95}Ba_{0.05}NiO_{4+\delta}$	PB5N| BZCYYb35 (25 μm) | Ni-BZCYYb35	600	Air (50% H_2O) vs. H_2 (3% H_2O)	~0.35	Not reported	90
$Pr_{1.95}Ba_{0.05}NiO_{4+\delta}$	PB5N-BZCD35| BZCD35 (25 μm) | Ni-BZCD35	600	Air (30% H_2O) vs. H_2 (3% H_2O)	0.61	0.5% for 60 h, 1.3 V at 600 °C	91
$Sr_{2.8}La_{0.2}Fe_2O_{7-\delta}$	SLF| BZCY35 (20 μm) | Ni-BZCY35	600	Air (20% H_2O) vs. H_2 (3% H_2O)	0.46	No degradation for 30 h, 0.21 A cm⁻² at 650 °C	92
$SrEu_2Fe_{1.8}Co_{0.2}O_{7-\delta}$	SEFC-BZCY17| BZCY17 (15 μm) | Ni-BZCY17	600	Air (10% H_2O) vs. H_2 (3% H_2O)	0.42	No degradation for 230 h, 1.3 V at 600 °C	70
$SrEu_2Fe_{1.8}Co_{0.2}O_{7-\delta}$	SEFC| BZY20 (15 μm) | Ni-BZY20	600	Air (10% H_2O) vs. H_2	0.76	No degradation for 100 h, 0.8 A cm⁻² at 550 °C	93
$Y_{0.8}Er_{0.2}BaCo_{3.2}Ga_{0.8}O_{7+\delta}$	YEBCG-BZCYYb1711| BZCYYb1711 (14 μm) | Ni-BZCYYb1711	600	Air (20% H_2O) vs. N_2 (10% H_2)	~1.2	No degradation for 1000 h reversible operation, 0.2 A cm⁻² at 600 °C	94
$Ca_3Co_4O_{9+\delta}$	Ca$_3$Co$_4$O$_{9+\delta}$| BZCY35 (25 μm) | Ni-BZCY35	600	Air (1% H_2O) vs. H_2 (3% H_2O)	0.293	Stable for 1500 h, OCV at 700 °C	95
$Ba_3(MnO_4)_2$-$Sb_{0.05}Sn_{0.95}O_{2-\delta}$	Ba$_3$(MnO$_4$)$_2$-Sb$_{0.05}$Sn$_{0.95}$O$_{2−\delta}$ (1.2 mm) | Pt	700	Air (20% H_2O) vs. Ar (5% H_2)	~0.05	Not reported	96

Note: YSZ: $(Y_2O_3)_{0.08}(ZrO_2)_{0.92}$; SDC: $Ce_{0.8}Sm_{0.2}O_{1.9}$, GDC: $Ce_{0.9}Gd_{0.1}O_{1.95}$, BZY20: $BaZr_{0.8}Y_{0.2}O_{3-\delta}$, BZCY17: $BaZr_{0.1}Ce_{0.7}Y_{0.2}O_{3-\delta}$, BZCY26: $BaZr_{0.2}Ce_{0.6}Y_{0.2}O_{3-\delta}$, BZCY35: $BaZr_{0.3}Ce_{0.5}Y_{0.2}O_{3-\delta}$, BZCY44: $BaZr_{0.4}Ce_{0.4}Y_{0.2}O_{3-\delta}$, BZCY(54)$_{8/9}$2: $BaZr_{0.44}Ce_{0.36}Y_{0.2}O_{3-\delta}$, BZCY72: $BaZr_{0.7}Ce_{0.2}Y_{0.1}O_{3-\delta}$, BZCY36: $BaZr_{0.3}Ce_{0.6}Y_{0.1}O_{3-\delta}$, BZCYZ: $BaCe_{0.5}Zr_{0.3}Y_{0.16}Zn_{0.04}O_{3-\delta}$, BZCYYb1711: $BaZr_{0.1}Ce_{0.7}Y_{0.1}Yb_{0.1}O_{3-\delta}$, BZCYYb3511: $BaZr_{0.3}Ce_{0.5}Y_{0.1}Yb_{0.1}O_{3-\delta}$, BZCYYb4411: $BaZr_{0.4}Ce_{0.4}Y_{0.1}Yb_{0.1}O_{3-\delta}$, BZCYYC2: $BaCe_{0.68}Zr_{0.1}Y_{0.1}Yb_{0.1}Cu_{0.02}O_{3-\delta}$, BZCYYbGd: $BaCe_{0.5}Zr_{0.2}Y_{0.1}Yb_{0.1}Gd_{0.1}O_{3-\delta}$, BHCYYb3511: $BaHf_{0.3}Ce_{0.5}Y_{0.1}Yb_{0.1}O_{3-\delta}$, BCZYSm: $BaCe_{0.7}Zr_{0.1}Y_{0.1}Sm_{0.1}O_{3-\delta}$, BZCD35: $BaZr_{0.3}Ce_{0.5}Dy_{0.2}O_{3-\delta}$, BCZI3: $BaCe_{0.5}Zr_{0.2}In_{0.3}O_{3-\delta}$, SZCY: $SrZr_{0.5}Ce_{0.4}Y_{0.1}O_{3-\delta}$, FL: functional layer. The abbreviation of air electrode materials is corresponding to each other.
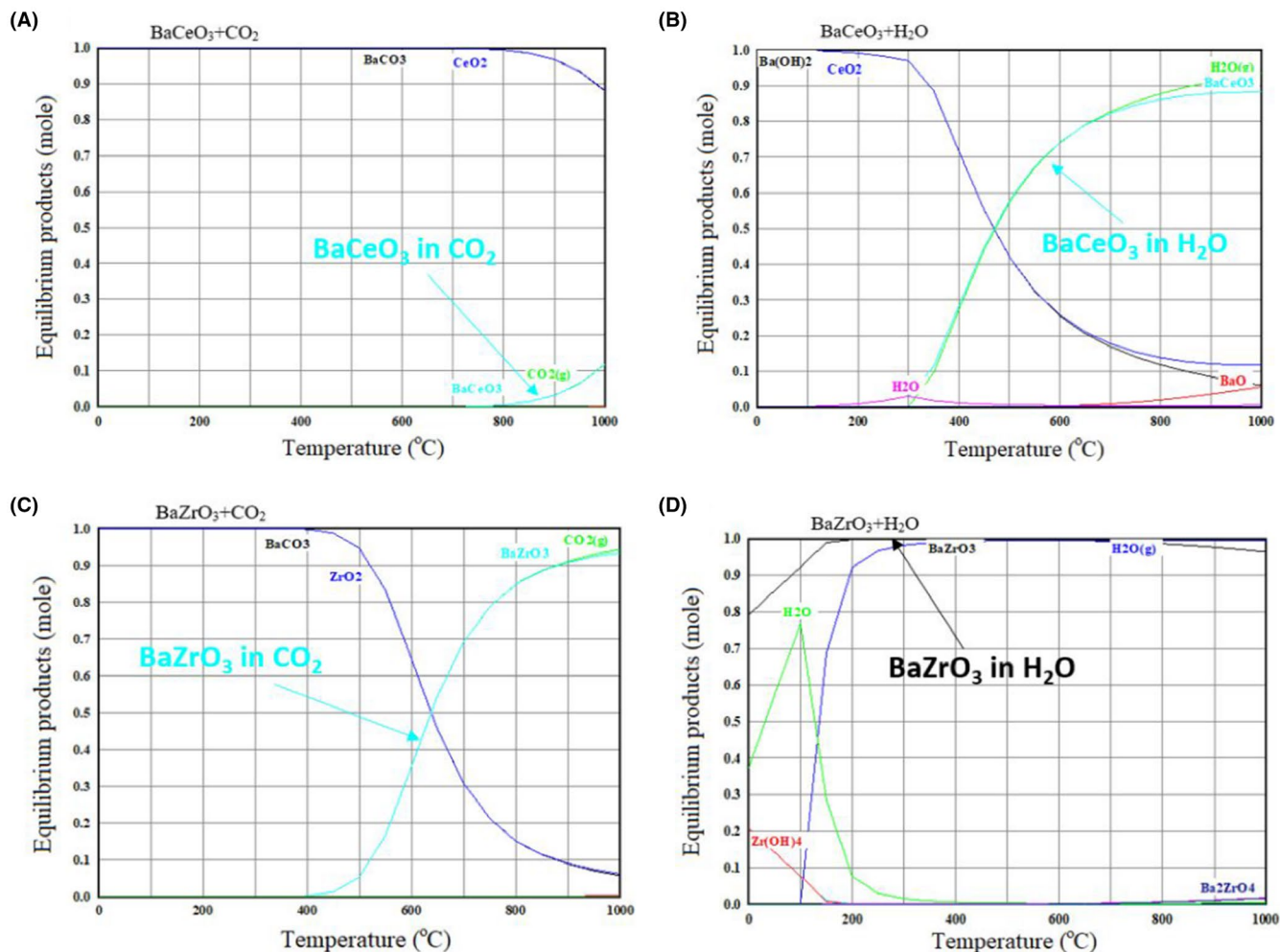
(A)

(B)

(C)

(D)

FIGURE 4 Equilibrium products between (A) $BaCeO_3$ and CO_2, (B) $BaCeO_3$ and H_2O, (C) $BaZrO_3$ and CO_2, (D) $BaZrO_3$ and H_2O. The amount of each reactant is 1 mole. Reprinted with permission from Ref.[35] Copyright 2020 American Chemical Society

$BaCeO_3$ and $BaZrO_3$ are not thermodynamically stable at lower temperatures. The $BaCeO_3$ can be decomposed by the chemical reaction with steam, leading to degradation of total cell performance. For example, the current density of a PCEC with a ~15-μm-thick Ce-rich $BaCe_{0.8}Zr_{0.2}O_{3-\delta}$ electrolyte decrease by ~9% under 10-hour short-term operation at 1.1 V.[36] Fortunately, the $BaZrO_3$ is relatively stable at typical PCEC operation conditions due to its low reaction kinetics with H_2O or CO_2,[15] which was further supported by no phase change of the Zr-rich $BaZr_{0.8}Y_{0.2}O_{3-\delta}$ (BZY20) film after treatment in boiling water or steam at 600°C.[37]

The hydration of the proton conductors leads not only to the phase transitions but also to the lattice expansion. The chemical expansion is influenced by the basicity of oxides and the amount of the acceptor dopant.[17] A high degree of expansion could cause the mechanical stress and deteriorates the conductivity and the contact between electrolyte and electrode. For example, the ohmic resistance (R_o) of a chemical stable BZY20 electrolyte increased after 80-h operation at 1.3 V and 600°C.[38]

Except for chemical instability and expansion, the BaO evaporation and redistribution of the acceptor dopants between A-site and B-site during high-temperature operation also affect the concentration of oxygen vacancies and subsequent proton conductivity.[17] Sintering aids are commonly used for reducing the sintering temperature and increase grain sizes of $BaZrO_3$-based electrolytes. However, the sintering aids (ie, NiO) may induce mechanical degradation of BZY due to the reduction of NiO at the grain boundaries.[39]

3.1.2 | Modification strategies of proton-conducting electrolytes

Modifying the chemical composition of the Ba-based proton conductors is the key strategy to balance their chemical stability and conductivity. The BZCYYb4411 with a ratio of Zr: Ce = 4:4 showed good chemical stability in the presence of CO_2 and H_2O, enabling minimal deterioration

of the conductivity and sinterability in comparison with the Ce-rich case.[32,40-42]

To further improve the stability of the Ba-based proton conductor, Murphy et al proposed the replacement of zirconium in BZCYYb with hafnium (Hf) to form $BaHf_xCe_{0.8-x}Y_{0.1}Yb_{0.1}O_{3-\delta}$ (BHCYYb).[43] The $BaHfO_3$ has a higher Gibbs free energy for the reaction with H_2O and CO_2 than $BaZrO_3$, suggesting potentially higher chemical stability (Figure 5A). The X-ray diffraction (XRD) spectra showed no obvious phase change of BHCYYb ($x = 3$ or 4) after the long-term conductivity measurement in 25% CO_2, 25% H_2O, and 50% H_2 for 500 hours at 700°C (Figure 5B). As a result, no obvious degradation was observed for the PCEC with $BaHf_{0.3}Ce_{0.5}Y_{0.1}Yb_{0.1}O_{3-\delta}$ (BHCYYb3511) as electrolyte and PBSCF as air electrode after 1000 hours operation at a current density of 1 A cm^{-2} at 600°C (Figure 5C).

The chemical stability of a perovskite oxide can be enhanced by optimizing the tolerance factor closer to 1 for an energetically favorable cubic structure.[24] Partial substitution of B-site ions of proton conductors with acceptor dopants can decrease the basicity for increasing tolerance factor and thus improve their stability. For example, Rajendran et al reported a tri-doped $BaCeO_3$-$BaZrO_3$ by

partially substituting Zr with Y, Yb, and gadolinium (Gd), forming $BaCe_{0.5}Zr_{0.2}Y_{0.1}Yb_{0.1}Gd_{0.1}O_{3-\delta}$ (BCZYYbGd).[44] XRD spectra showed that the BCZYYbGd electrolyte was stable over 200 hours at 50 vol % steam in argon and 600°C (Figure 5D). This was attributed to the higher electronegativity value of Gd (1.20) compared to that of the host Ce (1.12), which stabilizes the crystal structure and minimizes the dopant−hydroxyl interaction. Therefore, only 1.7% degradation was observed for a BCZYYbGd-based PCEC after 200 hours operation at 1.3 V, 600°C, and 20% moisture.

Incorporation of a small amount of transition metals into a Ba-based proton conductor was found to largely improve its sinterability and stability. For example, introducing Cu^{2+} into the interstitial position of BZCYYb1711 forms $BaCe_{0.68}Zr_{0.1}Y_{0.1}Yb_{0.1}Cu_{0.02}O_{3-\delta}$ (BCZYYC2), leading to excellent chemical stability at high-temperature and high-humidity conditions.[45] Furthermore, no degradation was found for the BCZYYC2 cell during a 60-h reversible operation and the R_o remained almost constant (Figure 5E). Iron-doped $BaZr_{0.1}Ce_{0.7}Y_{0.2}O_{3-\delta}$ (BZCY17) was stable during 25-hour operation with 100% H_2O at 400°C,[35] whereas the pristine BZCY17 decomposed to

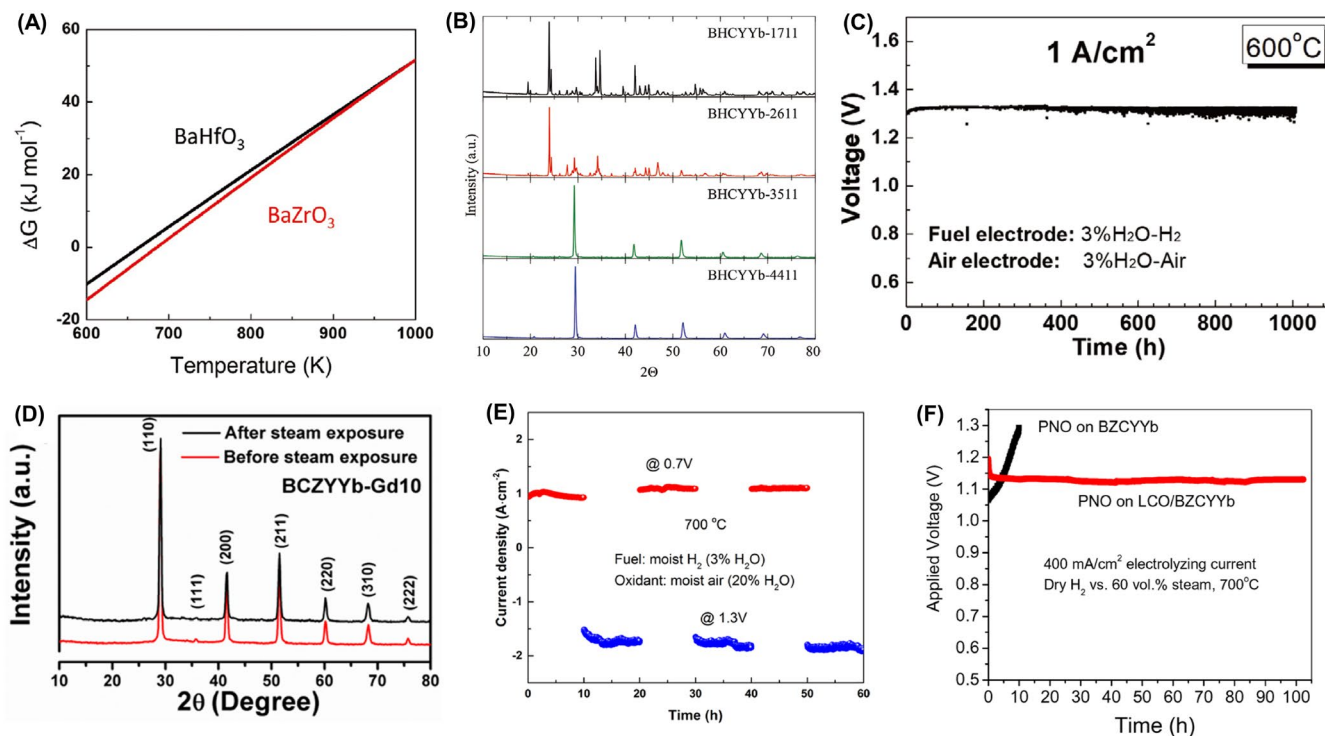**FIGURE 5** (A) Gibbs free energy of the reaction between $BaZrO_3$ or $BaHfO_3$ and CO_2 to form $BaCO_3$ and ZrO_2 or HfO_2. (B) XRD patterns of BHCYYb after exposure to 25% CO_2, 25% H_2O, and 50% H_2 at 700°C for 500 h.[43] (C) Long-term stability of the BHCYYb electrolysis cell at 600°C and 1 A cm^{-2}. Figures 5A-C were reprinted with permission from Ref.[43] Copyright 2020 John Wiley and Sons. (D) XRD patterns of the BCZYYbGd film before and after exposure to 50 vol.% steam in argon at 600°C for 200 h. Reprinted with permission from Ref.[44] Copyright 2020 American Chemical Society. (E) The current density of the BCZYYC2 cell as a function of time tested at 700°C with a pulse voltage. Reprinted with permission from Ref.[45] Copyright 2018 American Chemical Society. (F) Stability of PCEC with or without and $La_2Ce_2O_7$ (LCO) layer. Reprinted with permission from Ref.[48] Copyright 2019 American Chemical Society

Ba(OH)$_2$, CeO$_2$, and Y$_2$O$_3$ only after 5 hours test. The improved stability was attributed to the relatively high thermodynamic stability of the BaFeO$_3$ phase.

A-site deficiency can increase stability against carbonate formation in Ba-based perovskites.[46] As reported by Kim et al, when submerged in water at 90°C, a 5%-Ba-deficient Ba$_{0.95}$Ce$_{0.9}$Dy$_{0.1}$O$_{3-\delta}$ sintered pellet was stable, whereas BaCe$_{0.9}$Dy$_{0.1}$O$_{3-\delta}$ rapidly collapsed.[47] This happened probably because the reduced basicity of doped BaCeO$_3$ suppressed the formation of intergranular amorphous phases.

Another approach is the physical isolation of an electrolyte from the H$_2$O or CO$_2$ by forming a protective layer at the electrolyte/electrode interface. Li et al coated a ~10-μm-thick La$_2$Ce$_2$O$_7$ layer onto the BZCYYb1711 electrolyte to prepare a bilayer electrolyte, because the La$_2$Ce$_2$O$_7$ possesses a moderate proton conductivity and higher tolerance toward water.[48] As shown in Figure 5F, the bilayer electrolyte cell maintained the constant electrolyzing potential of 1.13 V at an applied current density of 0.4 A cm^{-2} under high humidified condition (60 vol% water in air) for a 102-hour operation. In contrast, the cell without the protection of the La$_2$Ce$_2$O$_7$ layer decreased significantly from 1.29 V to 1.07 V only after a 10-hour operation.

Notably, the electrolyte stability can also be improved by tuning its morphology. For example, the Ce-rich BZCYYb1711 dense pellet exhibited a high resistance toward H$_2$O and CO$_2$, whereas BZCYYb1711 powder suffered a phase change mainly due to its large surface area exposed to the gasses.[27]

3.2 | Air electrode materials

Since the rate-limiting water oxidation reaction and OER occur at the air electrodes of PCECs, most of attentions have been focused on the design of air electrode materials.[9,15,18,24] Similar to protonic ceramic fuel cells (PCFCs), the air electrode in PCECs requires high electronic conductivity under an oxidizing atmosphere, excellent ionic conductivity, high catalytic activity, and good chemical compatibility with the electrolyte. Most importantly, high water tolerance and excellent phase and chemical stabilities should be considered for the sake of the long-term electrolysis operation.

For conventional SOECs, mixed oxygen ion and electron conductors (MIECs) were applied to air electrodes, such as La$_{0.8}$Sr$_{0.2}$MnO$_{3-\delta}$ (LSM), La$_{0.6}$Sr$_{0.4}$Co$_{0.2}$Fe$_{0.8}$O$_{3-\delta}$ (LSCF), and Ba$_{0.5}$Sr$_{0.5}$Co$_{0.8}$Fe$_{0.2}$O$_{3-\delta}$ (BSCF). For PCECs, triple ionic–electronic conductors (TIECs) with the capability of simultaneous transport of protons, oxygen ions, and holes were considered as idea air electrodes with a maximum of the TPB area.[24] In the TIECs, protons transport through vibrational and rotational motion (via the Grotthuss mechanism), the oxygen ions through vacancy diffusion, and electronic charge carriers through a bonding between aliovalent transition metal sites and oxygen ligands or a small-polaron hopping mechanism.[24] Generally, these TIECs have three types of structures, namely, perovskite (ABO$_3$), double-perovskite (AA'B$_2$O$_{5+\delta}$), and Ruddlesden–Popper (RP) oxide (A$_{n+1}$B$_n$O$_{3n+1}$) (Figure 6). Large alkaline-earth or rare-earth metal (eg, Ba, La, Sr, and Pr) is partially substituted into A-site to increase electronic conductivity.[15,24] Small tri- or tetravalent transition metal ions occupied in the B-site. The performance of these air electrode materials in PCECs for steam electrolysis was summarized in Table 2. As a representative perovskite-based TIEC, BaCo$_{0.4}$Fe$_{0.4}$Zr$_{0.1}$Y$_{0.1}$O$_{3-\delta}$ (BCFZY) was demonstrated to have higher proton conductivity, thus achieving a quite lower polarization resistance of 0.13 Ω cm^2 and a high electrolysis current density of ~1 A cm^{-2} at 1.3 V at 600°C.[27] Double perovskite oxide PBSCF exhibited high electronic conductivity, good water uptake capability, and fast migration of relevant ionic defects, leading to excellent performance of its PCEC cell for steam electrolysis (1.80 A cm^{-2} at 1.3 V at 600°C).[32,40] The layered Ln$_2$NiO$_{4+\delta}$ (Ln = La, Nd, and Pr) nickelates with RP structure have gained more interest as air electrodes in PCECs due to their triple-conducting properties and high oxygen diffusion.[25] One notable La$_{1.2}$Sr$_{0.8}$NiO$_{4-\delta}$ (LSN) infiltrated BCZYYC2 air electrode yielded a large electrolysis current density of 3.02 A cm^{-2} at 1.3 V at 700°C.[49]

3.2.1 | Degradation of air electrodes

The challenge of the air electrode of PCEC is the chemical stability under highly humidified conditions. The degradation of air electrodes in PCECs is mainly caused by phase change, chemical incompatibility, and cation interdiffusion.[15,17,25]

Similar to the electrolytes, the alkaline-earth cations in the A-site of air electrodes may deteriorate their phase stability toward H$_2$O and CO$_2$. For example, Duan et al attributed the degradation of the PCEC under 1200 hours of continuous operation with 10% steam to the slight phase instability of the BCFZY air electrodes under hydrothermal conditions based on the EIS measurements.[27] The degradation became more severe with increasing steam concentration to 78%. Another double-perovskite air electrode, Ba$_{1-x}$Gd$_{0.8}$La$_{0.2+x}$Co$_2$O$_{6-\delta}$ (BGLC), exhibits excellent performance at high steam concentration with $x < 0.5$.[50] However, a secondary phase of hexagonal BaCoO$_3$ was observed under 1.5 bar of steam at 600°C for 72 hours. Furthermore, the Pr$_2$NiO$_{4+\delta}$ phase easily
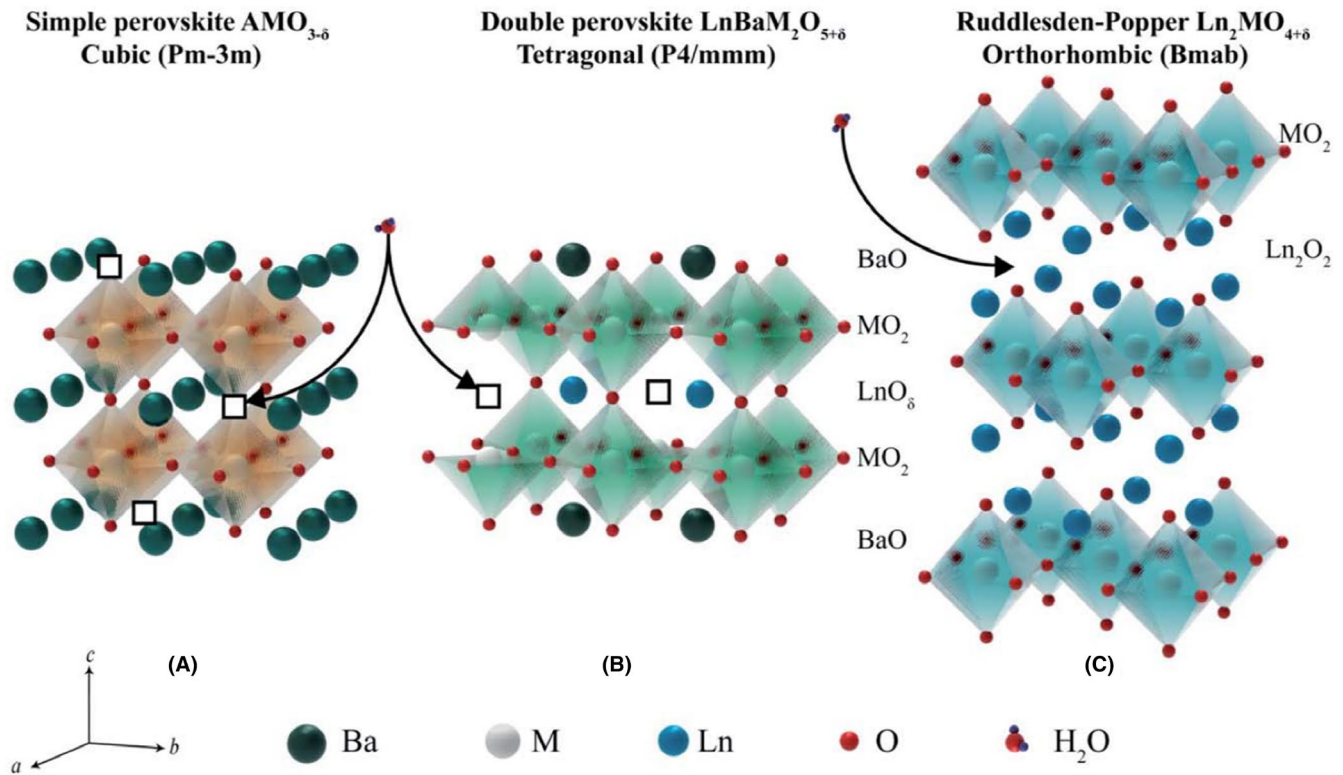
FIGURE 6 The different structures of the air electrode materials in PCECs. The arrow was indicated the possible water insertion sites. Reprinted with permission from Ref.[25] Copyright 2021 Royal Society of Chemistry

decomposes under oxidizing conditions due to its undesirable low-pO_2 stability boundary compared to $La_2NiO_{4+\delta}$ and $Nd_2NiO_{4+\delta}$.[25] This intrinsic instability cannot be improved by B-site substitutions of Pr with alkaline-earth cations.[25]

Most of the air electrodes in PCECs are cobalt-based oxides because of their high electronic conductivity and OER activity. However, the cobalt-based electrodes suffer from thermo-mechanical incompatibility, which consequently reduces the thermo-cycling and the long-term operational stability of the PCECs. For example, the thermal expansion coefficient (TEC) of the state-of-the-art BSCF, PBSCF, and BCFZY air electrodes are 2.32×10^{-5} K^{-1}, 2.37×10^{-5} K^{-1}, and 2.16×10^{-5} K^{-1}, respectively.[15,40,51] However, the TEC values of the widely used protonic conductors are in the range of $(0.8\text{-}1.2) \times 10^{-5}$ K^{-1}.[9] Along with the TEC mismatching, this strain might cause cracking and delamination at the electrode/electrolyte interface.

Cation interdiffusion was found between conventional MIECs and proton conductors. For example, the formation of three interface layers was observed by X-ray micro-spectroscopy at the LSM-$BaCe_{0.8}Y_{0.2}O_{3-\delta}$ (BCY) interface after 72 hours of annealing at 1150°C.[52] The central phase was identified as a $BaMnO_3$, and the two other phases are Y-doped ceria, revealing the poor chemical and structural stability of the LSM/BCY couple.

Furthermore, a massive cation interdiffusion was found at the LSCF-BZY20 interface by secondary ions mass spectroscopy (SIMS), producing Kirkendall pores within the LSCF layer.[53] In addition, it was reported that the PCEC with a Fe_2O_3 modified LSM air electrode degraded fast with a 15% decrease in current density only after 10-hour electrolysis operation.[54] This poor stability was attributed to the cation interdiffusion between LSM and $BaCe_{0.5}Zr_{0.3}Y_{0.16}Zn_{0.04}O_{3-\delta}$ electrolyte.

3.2.2 | Modification strategies of air electrode materials

A-site cation doping can not only increase the hydration capability and oxygen vacancy concentration of the air electrode, but also enhance its phase stability. For example, the substitution of La in LSCF to Ba to form BSCF can suppress the strontium segregation in strontium cobalt ferrite due to the large ionic size of Ba^{2+} compared to Sr^{2+}.[15] Furthermore, it was revealed that replacing Sr in PBSCF air electrode with a relatively inert Ca enhanced its stability.[33] For conventional $LaMnO_3$-based cathodes, Ca-doped $LaMnO_3$ ($La_{0.5}Ca_{0.5}MnO_{3-\delta}$) demonstrates lower oxygen vacancy formation energy and lower protonation energy compared with Sr- or Ba-doped $LaMnO_3$.[55] The $La_{0.5}Ca_{0.5}MnO_{3-\delta}$ is also chemically stable against CO_2,

reflected by no phase change in 100-h treatment with 10% CO_2 air.

In addition to cation doping, the introduction of fluorine into the oxygen sublattice may be favorable for oxygen ionic transport and stability of RP structured air electrodes. As reported, the incorporation of fluorine into $Nd_{1.9}Ba_{0.1}NiO_{4+\delta}F_\gamma$ (γ = 0-0.10) solid solutions showed only a minor effect on the structural parameters without obvious microstructure change but led to a greater improvement in ion conductivity.[56]

Another strategy for obtaining high chemical stability is to eliminate alkaline-earth elements in the air electrode. Ding et al[42] reported an alkaline-earth-element-free triple-conducting $PrNi_{0.5}Co_{0.5}O_{3-\delta}$ (PNC) perovskite air electrode, which exhibited good chemical stability and interfacial connection with the electrolyte under higher steam concentrations (20 and 30%) for 100 hours. A similar air electrode $Pr_2NiO_{4+\delta}$ was also explored.[48,57] Furthermore, Xu et al reported a promising triple-conducting $La_{0.5}Sr_{0.5}Fe_{0.9}Mo_{0.1}O_{3-\delta}$ air electrode without involving basicity element or cobalt.[58] The theoretical studies indicated that Mo doping improves the proton migration and catalytic activity by tailoring the electronic structure of the neighboring atoms.

Tailoring the microstructure of the oxygen electrode is an effective way to avoid the gas diffusion limitation, decrease the steam starvation limitation, and reduce the partial pressure of the oxygen at the electrode/electrolyte interface. Wu et al reported a 3D PBSCF air electrode with hollow-fiber microstructure prepared using fabric textile as templates.[59] It was found that the current density of PCEC with 3D PBSCF was slightly increased at a constant 1.6 V applied voltage, whereas that of PCEC with conventional PBSCF decreased with time (Figure 7A). The improved performance was attributed to the redistribution of PBSCF particles to form a well-connected interface, increasing the active reaction area and thus promoting long-term stability (Figure 7B,C). The similar strategy was also exploited for fabricating a 3D PNC electrode.[42] The cell with 3D PNC showed no observable degradation over 220-hour operation at 1.4 V and 500°C.

The application of a functional layer between air electrode and electrolyte also gives benefit for enhancing electrolysis performance and stability. For example, a 100-nm-thin dense PBSCF layer was deposited by PLD to improve the contact between the air electrode and the electrolyte and maximize the surface activation and proton transport.[32] The PCEC with the configuration of PBSCF| PBSCF PLD| BZCYYb4411| Ni-BZCYYb4411 showed an unchanged current density and microstructure during 300-h operation at 1.3 V and 550°C.

The exsolution is the process that the active metal is incorporated into crystal structure during synthesis and forms stable active particles from the host support under operation, showing remarkable stability due to the stronger particle–support interactions.[21] Zhou et al observed in situ exsolved $BaCoO_{3-\delta}$ nanoparticles from PBCC air electrode after long-term PCEC operation by scanning electron microscopy (SEM) and transmission electron microscopy (TEM) with energy dispersive X-ray (EDX) analysis (Figure 7D).[33] The exsolved $BaCoO_{3-\delta}$ catalysts not only enhanced the OER activity and reduced the air electrode resistance but also ensured stability due to the strong interaction with the support. The degradation rates of the PCEC with the exsolved PBCC air electrode are 0.4, 4.0, and 3.3% per 1000 hours during the 800, 1500, and 1833 hours operations, respectively (Figure 7E). Furthermore, the PBCC air electrode showed high water tolerance under 50% H_2O atmosphere.

3.3 | Fuel electrode materials

The state-of-the-art fuel electrode material of the PCECs is the same as the PCFCs, namely, nickel-based cermet, in which the nickel served as electronic conductors and electrocatalysts and the ceramic support acts as proton conductors. To develop a highly stable fuel electrode in PCECs, experiences from the anode of PCFCs can be directly applied to that of PCECs, such as doping, infiltration/impregnation, in situ exsolution, and inserting a functional layer between fuel electrodes and electrolytes.[34] The most investigated fuel electrodes are Ni-BZY, Ni-BZCY, and Ni-BZCYYb, which would be selected according to the type of electrolytes. For a SOEC, the fuel electrodes are at risk of oxidizing in the presence of steam, which mainly accounts for cell degradation. For example, the TPB area of the YSZ-based SOEC decreases from 10.49 to 6.18 mm^{-2} after 1000 hours operation at 0.8 A cm^{-2} due to the Ni agglomeration and Ni migration from fuel electrode to the electrolyte.[60] Therefore, H_2 is commonly used as protective gas supplied with steam for the oxygen ion-conducting SOEC. However, the fuel electrode in PCEC is under a reducing atmosphere and is relatively stable during long-term electrolysis operation.

A possible issue of the fuel electrode in a PCEC is the Ni migration from the fuel electrode/electrolyte interface to the electrolyte. The diffusion of Ni was observed by field emission-electron probe microanalysis during co-sintering of the Ni-BZCYYb/BZCYYb couple.[61] Although the diffused Ni promoted the densification of BZCYYb electrolyte, it reduced the electrolyte intrinsic proton conductivity and consequently degrading the cell performances.

When the protonic ceramic cells operate under the reversible mode, the volume changes of the fuel electrodes
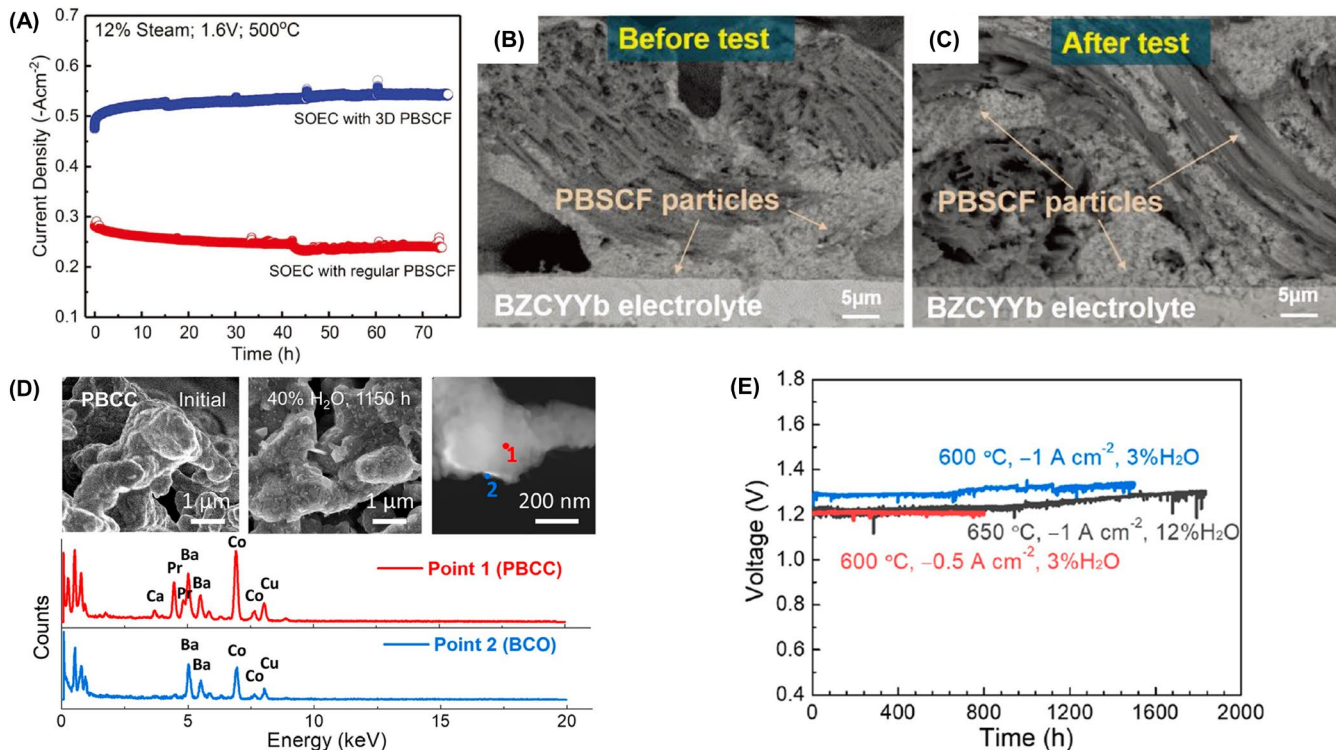
FIGURE 7 (A) Durability of PCECs with 3D PBSCF steam electrode (blue) and conventional PBSCF steam electrode (red) under applied voltage of 1.6 V at 500°C.[59] (B, C) SEM image near steam electrode/electrolyte interface before and after steam electrolysis. Figures 7A-C were reprinted with permission from Ref.[59] Copyright 2018 John Wiley and Sons. (D) SEM and TEM images of the PBCC electrodes before and after testing (1150 h, 700°C, 40% H_2O), and EDX spectra of point 1 and point 2, as marked in the TEM image.[33] (E) Long-term stability of PCECs with PBCC electrodes under different conditions. Figure 7D and 7E were reprinted with permission from Ref.[33] Copyright 2021 American Chemical Society

due to redox cycling of Ni to NiO lead to cell degradation. To solve this issue, Sun et al prepared an air-electrode-supported PCEC with a ~20-μm-thick Ni-BCZYYC2 fuel electrode.[62] The thin fuel electrode layer mitigated volume change under redox circle, and hence, the cell performance remained stable for 400-hour reversible operation (20 cycles of electrolysis mode at 1.1 V and fuel cell mode at 0.7 V). However, the electrolysis current density (83 mA cm^{-2} at 1.3 V at 600°C) is relatively lower than that of conventional fuel-electrode-supported PCECs with similar configurations (590 mA cm^{-2} at 1.3 V at 600°C),[45] which may result from water diffusion limitations in the thick air electrode structures. Therefore, rational design of the microstructure of electrodes is required to achieve the trade-off between performance and stability.

The exsolved nanoparticles are also beneficial to the stability of the fuel electrodes due to the strong metal–support interaction. The uniform distributed exsolved Ni particles were observed in the Ni-BZY20 fuel electrode after 600-hour operation under 20% steam.[27] The authors argued that the intimate contact between the exsolved Ni particles and the BZY20 support improves the stability of the PCEC.

Another option toward Ni-based cermet anode support is metal-supported PCEC, which was demonstrated better mechanical stability and tolerance to very rapid thermal cycling and redox cycling.[63] Moreover, the incorporation of the stainless-steel diffusion barrier inhibited diffusion of impurities in the sealant (eg, Si) into the fuel electrode and thus improved the cell's stability.[63]

4 | INFLUENCE OF THE OPERATING CONDITIONS

4.1 | Humidification

The steam concentration supply to the air electrode in lab-scale experiments ranges from 3% to 50% (Table 2). Generally, high water partial pressure leads to rapid material degradation and accelerate the microstructure change. For the electrolyte or air electrode containing alkaline-earth elements, the water vapor partial pressure leads to a wide variation of strain effects and thus chemical expansion.[17] Furthermore, water may catalyze the decomposition of perovskite oxides to base oxides,

increasing the formation of surface hydroxides and the mobility of impurities.[11] Consequently, a high degradation rate was observed for the PCEC under higher humifying conditions.[27,33] For example, the polarization resistances of PBSCF and $NdBa_{0.5}Sr_{0.5}Co_{1.5}Fe_{0.5}O_{5+\delta}$ air electrodes remained stable when exposed to 20% H_2O humidified air under a cyclic current (± 1 A cm^{-2}, 36 hours for each cycle), while increased significantly after exposure to 30% H_2O.[33] The degradation was ascribed to the aggravated Ba and Sr segregation under a high concentration of H_2O.

4.2 | Oxygen partial pressure

The partial pressure of oxygen (pO_2) would affect reaction kinetics, chemical stability, and ionic and electronic conductivities of air electrode and electrolyte materials. As shown in Figure 2C-H, higher pO_2 at the TPB decreases the proton or oxygen ion transport, but increases the hole concentration due to the parasitic oxidation reaction (Equation 10). This p-type electron transport in oxidizing conditions causes the electronic leakage of the proton-conducting electrolytes, reducing the Faradaic efficiency of the PCECs.[27] Recent studies demonstrated that a Ce-rich BZCYYb1711 has a much lower electronic charge carrier transference number than BZY20 because BZCYYb1711 favors hydration reaction and suppresses the parasitic oxidation reaction.[64,65] The pO_2 change can also induce a chemical strain for many air electrodes (eg, BCFZY, PBSCF), which results in the relative dimension shrinkage/expansion.[17] This mechanical stress further causes delamination at the electrode/electrolyte interface and deteriorates PECE stability.

4.3 | Polarization conditions

For conventional YSZ-based SOEC, the initial performance was found to degrade much faster in electrolysis mode than in fuel cell mode,[11] which would be the rapid degradation of the LSM-YSZ electrode at high current densities.[13] The current density significantly affects the structural degradation of the cells associated with the electrode overpotential.[5]

The PCECs also suffer from the polarization-dependent degradation. For example, a reversible protonic ceramic cell with $CaZr_{0.9}In_{0.1}O_{3-\delta}$ electrolyte showed a high degradation rate (18%) at 1.2 V applied voltage, whereas its performance remained unchanged at the fuel cell mode (0.8 V).[66] The different degradation behaviors were attributed to the unequal elementary reactions under different bias potential applications. Dailly et al evaluated the long-term durability of a $BaZr_{0.1}Ce_{0.8}Y_{0.1}O_{3-\delta}$-based
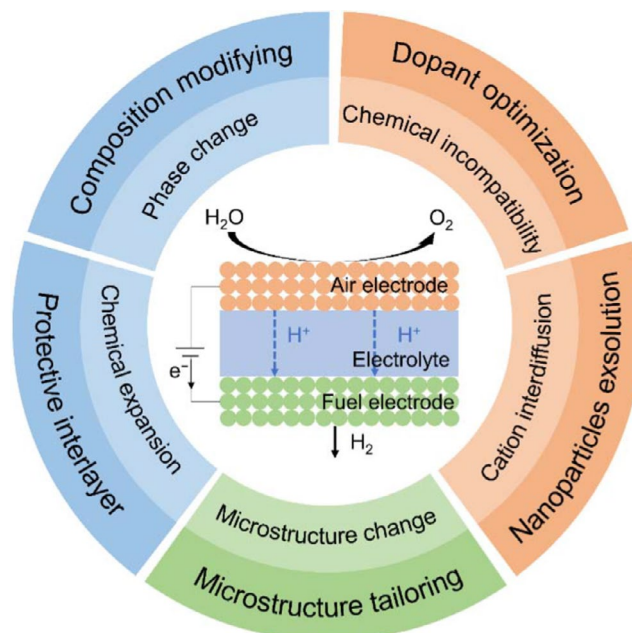

FIGURE 8 Degradation mechanisms and modification strategies for PCECs

protonic ceramic cell and found the degradation rate was only 1.2%/kh under fuel cell operation, while increased to 5-8%/kh under fuel cell/electrolysis reversible operation mode.[67]

Notably, the ohmic resistance of the PCECs decreased with increasing applied potentials due to the increase in electronic conductivity.[68-70] This may result from the n-type electronic conduction at the electrolyte–fuel electrode interface and the p-type electronic conduction at the electrolyte–air electrode interface.[69,71] Consequently, operating PCEC at high cell voltages may cause an issue of lower Faradaic efficiency.[15]

5 | CONCLUSION AND OUTLOOK

This review summarized the degradation evaluation, mechanism, and mitigation strategy in PCECs for steam electrolysis (Figure 8). Different from the oxygen ion-conducting SOEC, the degradation of PCEC is mainly due to the chemical instability, chemical expansion, fast microstructural changes, cationic interdiffusion, and segregation of electrolytes and air electrodes under highly humidified conditions.

The most important ceramic proton conductors are ABO_3-type perovskites based on the barium cerate ($BaCeO_3$) and barium zirconate ($BaZrO_3$). The proton conductors with Ba on the A-site exhibit high conductivity, but they are unstable in the presence of CO_2 and steam due to the undesirable reactions of Ba with the process gases. Modifying the chemical composition of the

Ba-based proton conductors is a main strategy to balance their chemical stability and conductivity. Forming a protective layer at the electrolyte/electrode interface to isolate the electrolyte from the process gases and tuning the electrolyte morphology are also employed to improve the stability of the electrolytes in PCECs.

Triple ionic–electronic conductors (TIECs) that can simultaneously transfer protons, oxygen ions and holes, are considered as idea air electrodes. These TIECs generally have three types of structures: perovskite (ABO_3), double-perovskite ($AA'B_2O_{5+\delta}$), and Ruddlesden–Popper (RP) oxide ($A_{n+1}B_nO_{3n+1}$). The main challenge of these air electrodes in PCECs is the chemical stability under highly humidified conditions. The degradation of air electrodes in PCECs is usually caused by phase change, chemical incompatibility, and cation interdiffusion. The composition modification of electrode materials is widely exploited to increase their stability. Tailoring the microstructures of air electrodes is also effective to solve some issues, such as the gas diffusion limitation and the steam starvation limitation. Furthermore, the exsolution can generate stronger particle–support interactions, leading to the increased stability.

Nickel-based cermet materials are commonly used as fuel electrodes for PCECs, mainly including Ni-BZY, Ni-BZCY, and Ni-BZCYYb. For the oxygen ion-conducting SOECs, H_2 is usually employed as protective gas. However, the fuel electrodes in PCECs, which are under a reducing atmosphere, exhibit relatively high stability during long-term electrolysis operation. Furthermore, the exsolved nanoparticles of fuel electrodes can increase their stability in PCECs due to the strong metal–support interaction. Other modification techniques can also improve the stability of fuel electrodes, such as doping, infiltration/impregnation, and inserting a functional layer between fuel electrodes and electrolytes.

More research efforts are needed to further improve the stability of PCECs. It is important to establish a fundamental composition–stability relationship for the perovskite proton conductors or air electrode materials with the assistant of theoretical calculations. This would become a scientific basis for the design of highly stable proton conductors and air electrodes. Adjusting the TECs for both electrolytes and electrodes can be used to inhibit mechanical degradation. The microstructures of the air electrode and interface between electrode and electrolyte are tunable for lowering the polarization resistance to improve the interface stability. The stability dependence of PCECs on the strong metal–support interaction generated from exsolution processes needs deep evaluation.

CONFLICTS OF INTEREST
The authors declare no competing financial interest.

ORCID
Yun Hang Hu https://orcid.org/0000-0002-5358-8667

REFERENCES
1. Turner JA. Sustainable hydrogen production. *Science*. 2004;305(5686):972-974.
2. Zhang L, Zhao H, Wilkinson DP, Sun X, Zhang J. *Electrochemical Water Electrolysis: Fundamentals and Technologies*. CRC Press; 2020.
3. Han B, Wei W, Li M, Sun K, Hu YH. A thermo-photo hybrid process for steam reforming of methane: highly efficient visible light photocatalysis. *Chem Commun*. 2019;55(54):7816-7819.
4. Hu YH, Ruckenstein E. Catalytic conversion of methane to synthesis gas by partial oxidation and CO_2 reforming. *Adv Catal*. 2004;48:297-345.
5. Ebbesen SD, Jensen SH, Hauch A, Mogensen MB. High temperature electrolysis in alkaline cells, solid proton conducting cells, and solid oxide cells. *Chem Rev*. 2014;114(21):10697-10734.
6. Chang L, Sun ZX, Hu YH. 1T phase transition metal dichalcogenides for hydrogen evolution reaction. *Electrochem Energ Rev*. 2021;4(2):194-218.
7. Hauch A, Kungas R, Blennow P, et al. Recent advances in solid oxide cell technology for electrolysis. *Science*. 2020;370(6513):eaba6118.
8. Bi L, Boulfrad S, Traversa E. Steam electrolysis by solid oxide electrolysis cells (SOECs) with proton-conducting oxides. *Chem Soc Rev*. 2014;43(24):8255-8270.
9. Lei L, Zhang J, Yuan Z, Liu J, Ni M, Chen F. Progress report on proton conducting solid oxide electrolysis Cells. *Adv Funct Mater*. 2019;29(37):1903805.
10. Moçoteguy P, Brisse A. A review and comprehensive analysis of degradation mechanisms of solid oxide electrolysis cells. *Int J Hydrogen Energy*. 2013;38(36):15887-15902.
11. Wang Y, Li W, Ma L, Li W, Liu X. Degradation of solid oxide electrolysis cells: phenomena, mechanisms, and emerging mitigation strategies—a review. *J Mater Sci Technol*. 2020;55:35-55.
12. Hauch A, Brodersen K, Chen M, et al. A decade of solid oxide electrolysis improvements at DTU energy. *ECS Trans*. 2017;75(42):3.
13. Schefold J, Poepke H, Brisse A. Solid oxide electrolyser cell testing up to the above 30,000 h time range. *ECS Trans*. 2020;97(7):553.
14. Li Z, Zhang H, Xu H, Xuan J. Advancing the multiscale understanding on solid oxide electrolysis cells via modelling approaches: a review. *Renew Sust Energ Rev*. 2021;141:110863.
15. Duan C, Huang J, Sullivan N, O'Hayre R. Proton-conducting oxides for energy conversion and storage. *Appl Phys Rev*. 2020;7(1):011314.
16. Bi L, Boulfrad S, Traversa E. Reversible solid oxide fuel cells (R-SOFCs) with chemically stable proton-conducting oxides. *Solid State Ionics*. 2015;275:101-105.
17. Wang W, Medvedev D, Shao Z. Gas humidification impact on the properties and performance of perovskite-type functional materials in proton-conducting solid oxide cells. *Adv Funct Mater*. 2018;28(48):1802592.

18. Medvedev D. Trends in research and development of protonic ceramic electrolysis cells. *Int J Hydrogen Energy*. 2019;44(49):26711-26740.

19. Ji HI, Lee JH, Son JW, Yoon KJ, Yang S, Kim BK. Protonic ceramic electrolysis cells for fuel production: a brief review. *J Korean Ceram Soc*. 2020;57(5):480-494.

20. Kasyanova AV, Tarutina LR, Rudenko AO, Lyagaeva JG, Medvedev DA. Ba (Ce, Zr) O_3-based electrodes for protonic ceramic electrochemical cells: towards highly compatible functionality and triple-conducting behaviour. *Russ Chem Rev*. 2020;89(6):667.

21. Irvine JTS, Neagu D, Verbraeken MC, Chatzichristodoulou C, Graves C, Mogensen MB. Evolution of the electrochemical interface in high-temperature fuel cells and electrolysers. *Nat. Energy*. 2016;1(1):1-13.

22. Skinner SJ. Recent advances in the understanding of the evolution of surfaces and interfaces in solid oxide cells. *Adv Mater Interfaces*. 2019;6(15):1900580.

23. Chiara A, Giannici F, Pipitone C, et al. Solid-solid interfaces in protonic ceramic devices: a critical review. *ACS Appl Mater Interfaces*. 2020;12(50):55537-55553.

24. Papac M, Stevanovic V, Zakutayev A, O'Hayre R. Triple ionic-electronic conducting oxides for next-generation electrochemical devices. *Nat Mater*. 2021;20(3):301-313.

25. Tarutin AP, Lyagaeva JG, Medvedev DA, Bi L, Yaremchenko AA. Recent advances in layered $Ln_2NiO_{4+\delta}$ nickelates: fundamentals and prospects of their applications in protonic ceramic fuel and electrolysis cells. *J Mater Chem A*. 2021;9(1):154-195.

26. Buttler A, Spliethoff H. Current status of water electrolysis for energy storage, grid balancing and sector coupling via power-to-gas and power-to-liquids: a review. *Renew Sust Energ Rev*. 2018;82:2440-2454.

27. Duan C, Kee R, Zhu H, et al. Highly efficient reversible protonic ceramic electrochemical cells for power generation and fuel production. *Nat Energy*. 2019;4(3):230-240.

28. Wang H, Wang X, Meng B, et al. Perovskite-based mixed protonic–electronic conducting membranes for hydrogen separation: recent status and advances. *J Ind Eng Chem*. 2018;60:297-306.

29. Ni M, Shao Z. Fuel cells that operate at 300° to 500°C. *Science*. 2020;369(6500):138-139.

30. He F, Song D, Peng R, Meng G, Yang S. Electrode performance and analysis of reversible solid oxide fuel cells with proton conducting electrolyte of $BaCe_{0.5}Zr_{0.3}Y_{0.2}O_{3-\delta}$. *J Power Sources*. 2010;195(11):3359-3364.

31. Tian H, Li W, Ma L, et al. Deconvolution of water-splitting on the triple-conducting Ruddlesden-Popper-phase anode for protonic ceramic electrolysis cells. *ACS Appl Mater Interfaces*. 2020;12(44):49574-49585.

32. Choi S, Davenport TC, Haile SM. Protonic ceramic electrochemical cells for hydrogen production and electricity generation: exceptional reversibility, stability, and demonstrated faradaic efficiency. *Energy Environ Sci*. 2019;12(1):206-215.

33. Zhou Y, Liu E, Chen Y, et al. An active and robust air electrode for reversible protonic ceramic electrochemical cells. *ACS Energy Lett*. 2021;1511-1520.

34. Zhang W, Hu YH. Progress in proton-conducting oxides as electrolytes for low-temperature solid oxide fuel cells: from materials to devices. *Energy Sci Eng*. 2021;9(7):984-1011.

35. Liu Z, Chen M, Zhou M, et al. Multiple effects of iron and nickel additives on the properties of proton conducting yttrium-doped barium cerate-zirconate electrolytes for high-performance solid oxide fuel cells. *ACS Appl Mater Interfaces*. 2020;12(45):50433-50445.

36. Yang S, Wen Y, Zhang S, Gu S, Wen Z, Ye X. Performance and stability of $BaCe_{0.8−x}Zr_{0.2}In_xO_{3−\delta}$-based materials and reversible solid oxide cells working at intermediate temperature. *Int J Hydrogen Energy*. 2017;42(47):28549-28558.

37. Bi L, Shafi SP, Traversa E. Y-doped $BaZrO_3$ as a chemically stable electrolyte for proton-conducting solid oxide electrolysis cells (SOECs). *J Mater Chem A*. 2015;3(11):5815-5819.

38. Bi L, Traversa E. Steam electrolysis by proton-conducting solid oxide electrolysis cells (SOECs) with chemically stable $BaZrO_3$-based electrolytes. *ECS Trans*. 2015;68(1):3387.

39. Li J, Wang C, Wang X, Bi L. Sintering aids for proton-conducting oxides–a double-edged sword? A mini review. *Electrochem Commun*. 2020;112:106672.

40. Choi S, Kucharczyk CJ, Liang Y, et al. Exceptional power density and stability at intermediate temperatures in protonic ceramic fuel cells. *Nat Energy*. 2018;3(3):202-210.

41. Tang W, Ding H, Bian W, et al. Understanding of A-site deficiency in layered perovskites: promotion of dual reaction kinetics for water oxidation and oxygen reduction in protonic ceramic electrochemical cells. *J Mater Chem A*. 2020;8(29):14600-14608.

42. Ding H, Wu W, Jiang C, et al. Self-sustainable protonic ceramic electrochemical cells using a triple conducting electrode for hydrogen and power production. *Nat Commun*. 2020;11(1):1907.

43. Murphy R, Zhou Y, Zhang L, et al. A new family of proton-conducting electrolytes for reversible solid oxide cells: $BaHf_xCe_{0.8−x}Y_{0.1}Yb_{0.1}O_{3−\delta}$. *Adv Funct Mater*. 2020;30(35):2002265.

44. Rajendran S, Thangavel NK, Ding H, Ding Y, Ding D, Reddy Arava LM. Tri-doped $BaCeO_3$-$BaZrO_3$ as a chemically stable electrolyte with high proton-conductivity for intermediate temperature solid oxide electrolysis cells (SOECs). *ACS Appl Mater Interfaces*. 2020;12(34):38275-38284.

45. Yang S, Zhang S, Sun C, Ye X, Wen Z. Lattice incorporation of Cu^{2+} into the $BaCe_{0.7}Zr_{0.1}Y_{0.1}Yb_{0.1}O_{3-\delta}$ electrolyte on boosting its sintering and proton-conducting abilities for reversible solid oxide cells. *ACS Appl Mater Interfaces*. 2018;10(49):42387-42396.

46. Guo Y, Ran R, Shao Z, Liu S. Effect of Ba nonstoichiometry on the phase structure, sintering, electrical conductivity and phase stability of $Ba_{1±x}Ce_{0.4}Zr_{0.4}Y_{0.2}O_{3−\delta}$ ($0 \leq x \leq 0.20$) proton conductors. *Int J Hydrogen Energy*. 2011;36(14):8450-8460.

47. Kim HS, Bae HB, Jung W, Chung SY. Manipulation of nanoscale intergranular phases for high proton conduction and decomposition tolerance in $BaCeO_3$ polycrystals. *Nano Lett*. 2018;18(2):1110-1117.

48. Li W, Guan B, Ma L, Tian H, Liu X. Synergistic coupling of proton conductors $BaZr_{0.1}Ce_{0.7}Y_{0.1}Yb_{0.1}O_{3-\delta}$ and $La_2Ce_2O_7$ to create chemical stable, interface active electrolyte for steam electrolysis cells. *ACS Appl Mater Interfaces*. 2019;11(20):18323-18330.

49. Sun C, Yang S, Lu Y, Wen J, Ye X, Wen Z. Tailoring a micro-nanostructured electrolyte-oxygen electrode interface for proton-conducting reversible solid oxide cells. *J Power Sources*. 2020;449:227498.

50. Vollestad E, Strandbakke R, Tarach M, et al. Mixed proton and electron conducting double perovskite anodes for stable

and efficient tubular proton ceramic electrolysers. *Nat Mater.* 2019;18(7):752-759.

51. Zhou W, Ran R, Shao Z. Progress in understanding and development of $Ba_{0.5}Sr_{0.5}Co_{0.8}Fe_{0.2}O_{3-\delta}$-based cathodes for intermediate-temperature solid-oxide fuel cells: a review. *J Power Sources.* 2009;192(2):231-246.

52. Giannici F, Chiara A, Canu G, Longo A, Martorana A. Interface solid-state reactions in $La_{0.8}Sr_{0.2}MnO_3/Ce_{0.8}Sm_{0.2}O_2$ and $La_{0.8}Sr_{0.2}MnO_3/BaCe_{0.9}Y_{0.1}O_3$ disclosed by X-ray microspectroscopy. *ACS Appl. Energy Mater.* 2019;2(5):3204-3210.

53. Jeffrey C, Yokokawa H, Develos-Bagarinao K, et al. Influence of electrolyte substrates on the Sr-segregation and $SrSO_4$ formation in $La_{0.6}Sr_{0.4}Co_{0.2}Fe_{0.8}O_{3-\delta}$ thin films. *MRS Commun.* 2019;9(1):236-244.

54. Li H, Chen X, Chen S, Wu Y, Xie K. Composite manganate oxygen electrode enhanced with iron oxide nanocatalyst for high temperature steam electrolysis in a proton-conducting solid oxide electrolyzer. *Int J Hydrogen Energy.* 2015;40(25):7920-7931.

55. Dai H, Xu X, Liu C, Ma C, Zhang Q, Bi L. Tailoring a $LaMnO_3$ cathode for proton-conducting solid oxide fuel cells: integration of high performance and excellent stability. *J Mater Chem A.* 2021;9(21):12553-12559.

56. Tarutin AP, Vdovin GK, Medvedev DA, Yaremchenko AA. Fluorine-containing oxygen electrodes of the nickelate family for proton-conducting electrochemical cells. *Electrochim Acta.* 2020;337:135808.

57. Li W, Guan B, Ma L, Hu S, Zhang N, Liu X. High performing triple-conductive $Pr_2NiO_{4+\delta}$ anode for proton-conducting steam solid oxide electrolysis cell. *J Mater Chem A.* 2018;6(37):18057-18066.

58. Xu X, Xu YS, Ma JM, et al. Tailoring electronic structure of perovskite cathode for proton-conducting solid oxide fuel cells with high performance. *J Power Sources.* 2021;489:229486.

59. Wu W, Ding H, Zhang Y, et al. 3D self-architectured steam electrode enabled efficient and durable hydrogen production in a proton-conducting solid oxide electrolysis cell at temperatures lower than 600°C. *Adv Sci.* 2018;5(11):1800360.

60. Lay-Grindler E, Laurencin J, Villanova J, et al. Degradation study by 3D reconstruction of a nickel–yttria stabilized zirconia cathode after high temperature steam electrolysis operation. *J Power Sources.* 2014;269:927-936.

61. Shimada H, Yamaguchi T, Sumi H, Yamaguchi Y, Nomura K, Fujishiro Y. Effect of Ni diffusion into $BaZr_{0.1}Ce_{0.7}Y_{0.1}Yb_{0.1}O_{3-\delta}$ electrolyte during high temperature co-sintering in anode-supported solid oxide fuel cells. *Ceram Int.* 2018;44(3):3134-3140.

62. Sun C, Li Y, Ye X, Wen Z. A robust air electrode supported proton-conducting reversible solid oxide cells prepared by low temperature co-sintering. *J Power Sources.* 2021;492:229602.

63. Tucker MC. Progress in metal-supported solid oxide electrolysis cells: a review. *Int J Hydrogen Energy.* 2020;45(46):24203-24218.

64. Zhu H, Ricote S, Duan C, O'Hayre RP, Tsvetkov DS, Kee RJ. Defect incorporation and transport within dense $BaZr_{0.8}Y_{0.2}O_{3-\delta}$ (BZY20) proton-conducting membranes. *J Electrochem Soc.* 2018;165(9):F581-F588.

65. Zhu H, Ricote S, Duan C, O'Hayre RP, Kee RJ. Defect chemistry and transport within dense $BaCe_{0.7}Zr_{0.1}Y_{0.1}Yb_{0.1}O_{3-\delta}$ (BCZYYb) proton-conducting membranes. *J Electrochem Soc.* 2018;165(10):F845-F853.

66. Ye X-F, Wen YB, Yang SJ, et al. Study of $CaZr_{0.9}In_{0.1}O_{3-\delta}$ based reversible solid oxide cells with tubular electrode supported structure. *Int J Hydrogen Energy.* 2017;42(36):23189-23197.

67. Dailly J, Ancelin M, Marrony M. Long term testing of BCZY-based protonic ceramic fuel cell PCFC: Micro-generation profile and reversible production of hydrogen and electricity. *Solid State Ionics.* 2017;306:69-75.

68. Marrony M, Dailly J. Advanced proton conducting ceramic cell as energy storage device. *J Electrochem Soc.* 2017;164(9):F988-F994.

69. Gan Y, Zhang J, Li Y, Li S, Xie K, Irvine JTS. Composite oxygen electrode based on LSCM for steam electrolysis in a proton conducting solid oxide electrolyzer. *J Electrochem Soc.* 2012;159(11):F763-F767.

70. Huan D, Shi N, Zhang L, et al. New, Efficient, and reliable air electrode material for proton-conducting reversible solid oxide cells. *ACS Appl Mater Interfaces.* 2018;10(2):1761-1770.

71. Danilov N, Lyagaeva J, Vdovin G, Pikalova E, Medvedev D. Electricity/hydrogen conversion by the means of a protonic ceramic electrolysis cell with $Nd_2NiO_{4+\delta}$-based oxygen electrode. *Energy Convers Manage.* 2018;172:129-137.

72. Kobayashi T, Kuroda K, Jeong S, et al. Analysis of the anode reaction of solid oxide electrolyzer cells with $BaZr_{0.4}Ce_{0.4}Y_{0.2}O_{3-\delta}$ electrolytes and $Sm_{0.5}Sr_{0.5}CoO_{3-\delta}$ anodes. *J Electrochem Soc.* 2018;165(5):F342-F349.

73. Wang N, Toriumi H, Sato Y, et al. $La_{0.8}Sr_{0.2}Co_{1-x}Ni_xO_{3-\delta}$ as the efficient triple conductor air electrode for protonic ceramic cells. *ACS Appl Energy Mater.* 2020;4(1):554-563.

74. Yoo Y, Lim N. Performance and stability of proton conducting solid oxide fuel cells based on yttrium-doped barium cerate-zirconate thin-film electrolyte. *J Power Sources.* 2013;229:48-57.

75. Saqib M, Lee J-I, Shin J-S, et al. Modification of oxygen-ionic transport barrier of $BaCo_{0.4}Zr_{0.1}Fe_{0.4}Y_{0.1}O_3$ steam (air) electrode by impregnating samarium-doped ceria nanoparticles for proton-conducting reversible solid oxide cells. *J Electrochem Soc.* 2019;166(12):F746-F754.

76. Meng Y, Gao J, Huang H, et al. A high-performance reversible protonic ceramic electrochemical cell based on a novel Sm-doped $BaCe_{0.7}Zr_{0.1}Y_{0.2}O_{3-\delta}$ electrolyte. *J Power Sources.* 2019;439:227093.

77. Rao Y, Zhong S, He F, Wang Z, Peng R, Lu Y. Cobalt-doped $BaZrO_3$: a single phase air electrode material for reversible solid oxide cells. *Int J Hydrogen Energy.* 2012;37(17):12522-12527.

78. Leonard K, Okuyama Y, Takamura Y, et al. Efficient intermediate-temperature steam electrolysis with Y: $SrZrO_3$–$SrCeO_3$ and Y: $BaZrO_3$–$BaCeO_3$ proton conducting perovskites. *J Mater Chem A.* 2018;6(39):19113-19124.

79. Song YF, Liu JP, Wang YH, et al. Nanocomposites: a new opportunity for developing highly active and durable bifunctional air electrodes for reversible protonic ceramic cells. *Adv. Energy Mater.* 2021;11(36):2101899.

80. Leonard K, Druce J, Thoreton V, Kilner JA, Matsumoto H. Exploring mixed proton/electron conducting air electrode materials in protonic electrolysis cell. *Solid State Ionics.* 2018;319:218-222.

81. Kim J, Jun A, Gwon O, et al. Hybrid-solid oxide electrolysis cell: a new strategy for efficient hydrogen production. *Nano Energy.* 2018;44:121-126.

82. Lei L, Tao Z, Wang X, Lemmon JP, Chen F. Intermediate-temperature solid oxide electrolysis cells with thin proton-conducting electrolyte and a robust air electrode. *J Mater Chem A.* 2017;5(44):22945-22951.

83. Lei L, Zhang J, Guan R, Liu J, Chen F, Tao Z. Energy storage and hydrogen production by proton conducting solid oxide electrolysis cells with a novel heterogeneous design. *Energy Convers Manage*. 2020;218:113044.

84. Danilov N, Tarutin A, Lyagaeva J, Vdovin G, Medvedev D. CO_2-promoted hydrogen production in a protonic ceramic electrolysis cell. *J Mater Chem A*. 2018;6(34):16341-16346.

85. Lyagaeva J, Danilov N, Vdovin G, et al. A new Dy-doped $BaCeO_3$–$BaZrO_3$ proton-conducting material as a promising electrolyte for reversible solid oxide fuel cells. *J Mater Chem A*. 2016;4(40):15390-15399.

86. Yang S, Lu Y, Wang Q, Sun C, Ye X, Wen Z. Effects of porous support microstructure enabled by the carbon microsphere pore former on the performance of proton-conducting reversible solid oxide cells. *Int J Hydrogen Energy*. 2018;43(43):20050-20058.

87. Fu L, Zhou J, Yang J, et al. Exsolution of Cu nanoparticles in $(LaSr)_{0.9}Fe_{0.9}Cu_{0.1}O_4$ Ruddlesden-Popper oxide as symmetrical electrode for solid oxide cells. *Appl Surf Sci*. 2020;511:145525.

88. Yang S, Wen Y, Zhang J, Lu Y, Ye X, Wen Z. Electrochemical performance and stability of cobalt-free $Ln_{1.2}Sr_{0.8}NiO_4$ (Ln=La and Pr) air electrodes for proton-conducting reversible solid oxide cells. *Electrochim Acta*. 2018;267:269-277.

89. Tarutin A, Lyagaeva J, Farlenkov A, et al. A Reversible protonic ceramic cell with symmetrically designed $Pr_2NiO_{4+\delta}$-based electrodes: fabrication and electrochemical features. *Materials (Basel)*. 2019;12(1):118.

90. Danilov N, Lyagaeva J, Vdovin G, Medvedev D. Multifactor performance analysis of reversible solid oxide cells based on proton-conducting electrolytes. *Appl Energy*. 2019;237:924-934.

91. Tarutin A, Kasyanova A, Lyagaeva J, Vdovin G, Medvedev D. Towards high-performance tubular-type protonic ceramic electrolysis cells with all-Ni-based functional electrodes. *J. Energy Chem*. 2020;40:65-74.

92. Huan D, Wang W, Xie Y, et al. Investigation of real polarization resistance for electrode performance in proton-conducting electrolysis cells. *J Mater Chem A*. 2018;6(38):18508-18517.

93. Shi N, Xie Y, Huan D, et al. Controllable CO_2 conversion in high performance proton conducting solid oxide electrolysis cells and the possible mechanisms. *J Mater Chem A*. 2019;7(9):4855-4864.

94. Shin J-S, Park H, Park K, et al. Activity of layered swedenborgite structured $Y_{0.8}Er_{0.2}BaCo_{3.2}Ga_{0.8}O_{7+\delta}$ for oxygen electrode reactions in at intermediate temperature reversible ceramic cells. *J Mater Chem A*. 2021;9(1):607-621.

95. Pikalova E, Kolchugin A, Koroleva M, Vdovin G, Farlenkov A, Medvedev D. Functionality of an oxygen $Ca_3Co_4O_{9+\delta}$ electrode for reversible solid oxide electrochemical cells based on proton-conducting electrolytes. *J Power Sources*. 2019;438:226996.

96. Toriumi H, Kobayashi T, Hinokuma S, et al. High-valence-state manganate(v) $Ba_3Mn_2O_8$ as an efficient anode of a proton-conducting solid oxide steam electrolyzer. *Inorg Chem Front*. 2019;6(6):1587-1597.